RICE UNIVERSITY

Optical Lever Measurement Accuracy for Off-Resonance Atomic Force Microscopy

by

R. Parker Eason

A THESIS SUBMITTED
IN PARTIAL FULFILLMENT OF THE
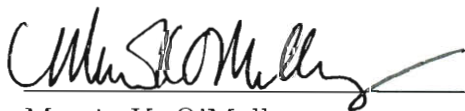REQUIREMENTS FOR THE DEGREE

Master of Science

APPROVED, THESIS COMMITTEE:

Andrew J. Dick, Chair
Assistant Professor of Mechanical
Engineering and Materials Science

Satish Nagarajaiah
Professor of Civil Engineering
and Mechanical Engineering

Marcia K. O'Malley
Associate Professor of Mechanical
Engineering and Materials Science

HOUSTON, TEXAS
APRIL 2011

Abstract

Optical Lever Measurement Accuracy for Off-Resonance Atomic Force Microscopy

by

R. Parker Eason

This research evaluates measurement accuracy in optical lever-based atomic force microscopy (AFM) for off-resonance conditions and parameter variations. Under controlled conditions and correct calibration, AFM provides researchers with the ability to accurately observe and manipulate matter on the micro- and nano-scale. Accuracy of imaging and nano-manipulation operations are directly correlated to the accuracy with which the displacement of the probe is measured. The optical lever method, a common displacement measurement technique employed in AFM, calculates probe displacement based on a calibration that assumes a consistent response profile throughout operation. Off-resonance excitation and tip-sample interaction forces during intermittent contact mode AFM can alter this response profile. Standard tapping-mode operation at the fundamental frequency is observed to be robust to changes in effective stiffness, maintaining accurate measurements for all laser spot positions considered. A nominal laser spot position between $Xp = 0.5$ and 0.6 is determined to most accurately predict displacement for off-resonance excitation during both free response and intermittent contact conditions. Measurement accuracy for off-resonance tapping- mode is more directly correlated to changes introduced to the interaction force profile than choice of spot position.

Acknowledgments

My sincere gratitude first and foremost goes to my advisor, Dr. Andrew J. Dick, who has been the guiding voice of my graduate studies while also allowing me the freedom to influence the direction of my research, a rare privilege for a graduate student. To my thesis committee, including Dr. Satish Nagarajaiah and Dr. Marcia K. O'Malley, I deeply appreciate you taking the time from your busy schedules. To my lab members, Quan Phan, Pooya Ghaderi and Wei Huang, I am always grateful for the helpful discussions and camaraderie during late nights at the lab. Much thanks to Rice University and the Mechanical Engineering and Materials Science department for giving me the opportunity to conduct my graduate studies at such a prestigious institution. Finally, thank you to my family for your loving support over the years.

Contents

List of Figures

List of Tables

Chapter 1

Introduction

The results in this thesis demonstrate how various parameter values influence optical lever measurement accuracy in off-resonance atomic force microscopy (AFM) by quantifying response profile deviations from the calibration conditions. Among the parameters studied, excitation frequency is determined to have a much more significant influence on response profile than tip-sample interactions have. As a result, amplitude modulation imaging is demonstrated to remain robust to variations in effective stiffness during operation, exhibiting less than 1 nm vertical measurement error for an increase of 10 times the effective stiffness. Probe displacement error is quantified based on operation conditions and spot position. Near-zero probe displacement measurement error is observed for nominal spot positions between $X_p = 0.5$ and 0.6.

This thesis is organized as follows. An overview of atomic force microscopy, the motivation for this work and a review of related studies are presented in the remainder of this chapter. The second chapter contains the derivation of governing equations and a description of how they are combined to produce a numerical model for simulating dynamic AFM operation. Results obtained under free response and intermittent contact conditions are presented in the third and fourth chapters, respectively. A

concluding summary of the problem and results is presented in the final chapter.

1.1 Motivation

For more than two decades, Atomic Force Microscopes (AFM) have been used to observe and manipulate matter on the micro- and nano-scale [1]. Whereas the spatial resolution of optical microscopes is limited to hundreds of nanometers by Abbe's diffraction law, atomic force microscopes have successfully achieved sub-nanometer imaging resolution [2]. Atomic force microscopy, alongside other methods such as scanning tunneling microscopy (STM), magnetic force microscopy (MFM) and electrostatic microscopy (ESM), developed from within the broader field of scanning probe microscopy (SPM) [3]. Scanning probe microscopes, in general, identify sample properties or topography by scanning a probe across the surface in close proximity, and measuring some interaction quantity between the probe and surface. Topographical representations of the surface can then be constructed from the measured interaction data [4].

As the name suggests, atomic force microscopes measure force interaction with the surface to perform imaging or manipulation operations. Main components central to AFM operation include a force effector, usually a small flexible probe with known stiffness, and means to identify the probe's deflection as it interacts with the sample surface. Cantilever probe shapes vary based on application, for example to promote or restrict torsional motion or to achieve a specific resonant frequency. Here we focus on one of the most common AFM system configurations, illustrated in Fig. 1.1.

This common configuration consists of a cantilever probe fixed at its base to a piezoelectric transducer, providing predictable deformation to allow precise control of the probe base movement. Attached to the free end of the probe is a sharp tip, ideally the only portion of the AFM system that interacts with the surface. A sharp tip
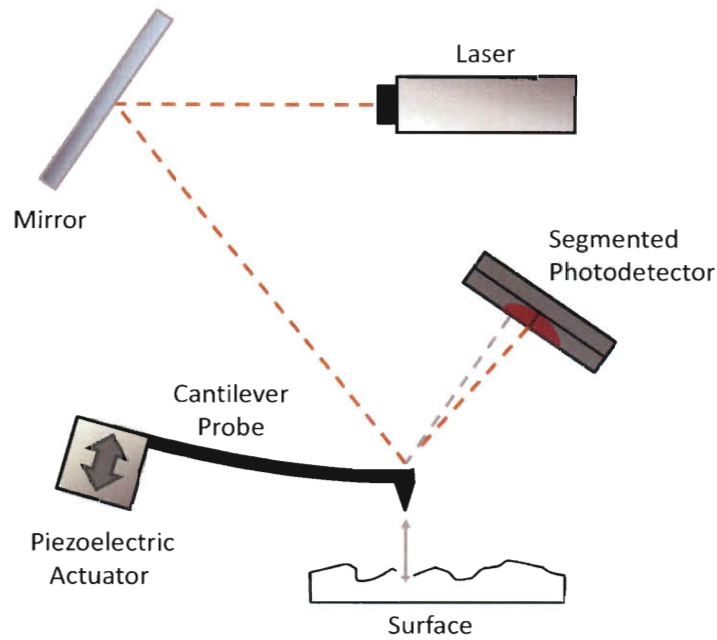
Figure 1.1: Schematic of the components that comprise the optical lever deflection measurement system in AFM.

minimizes the number of atoms that interact with the surface and therefore increases lateral resolution, though fracture is often experienced when operating very sharp tips on hard surfaces.

Imaging is performed by scanning the probe across a surface in the horizontal plane while controlling the vertical (z) height of the base to maintain close proximity between tip and surface. In contact mode operation, long- and short-range forces near the surface cause the probe to deflect proportional to the tip-surface separation. Feedback control seeks to achieve constant separation by maintaining constant deflection.

In dynamic operation, an AC voltage is applied at the piezoelectric material to harmonically oscillate the cantilever. Surface forces change the response behavior as the probe approaches the surface. Vertical z adjustments are made by the controller to maintain constant phase offset in non-contact AFM (NC-AFM) or constant re-

sponse amplitude in amplitude-modulation AFM (AM-AFM) [5, 6]. Dynamic modes generally offer an increased signal-to-noise ratio and can be less destructive to the sample surface.

At the micro- and nano- scale, methods to accurately measure probe displacement are limited. The first AFM systems utilized a scanning tunneling microscope to measure the deflection of the AFM probe [1]. Later designs employed piezoelectric crystals or piezo-resistive elements to measure the force corresponding to deflection [7]. The technique of interest to this work is the optical lever sensor, one of the most widely implemented methods today.

In the optical lever method, a laser is reflected off a point along the probe onto the surface of a segmented photo-diode detector. The photodetector returns a voltage signal corresponding to the difference between the amount of incident light detected by its two opposing vertical segments. Many photodetectors are segmented into quadrants, providing an additional difference signal between opposing horizontal segments to measure torsional motion of the cantilever. When the probe deflects, its change in slope alters the reflected position of the beam on the photodetector and the difference signal changes.

Figure 1.2 illustrates the changes observed by the photodetector as a deflection at the probe tip increases the slope at the surface of the probe. The probe has an initial deflection of zero with the laser spot centered on the photodetector, returning equal voltage readings from each quadrant (*i.e.* $1A = 1B = 2A = 2B = 5 \ Volts$). A deflection at the probe tip introduces an increase of $\Delta\theta$ to the probe's slope at the laser spot position, increasing the reflected angle of the laser proportional to the increase in slope and moving the incident spot upward on the photodetector. Since no torsional movement is introduced, the readings between the corresponding $A - B$ quadrants remain the same, whereas a voltage difference is introduced between the $1 - 2$ quadrants (*i.e.* $1A = 1B = 7 \ Volts$, $2A = 2B = 3 \ Volts$).
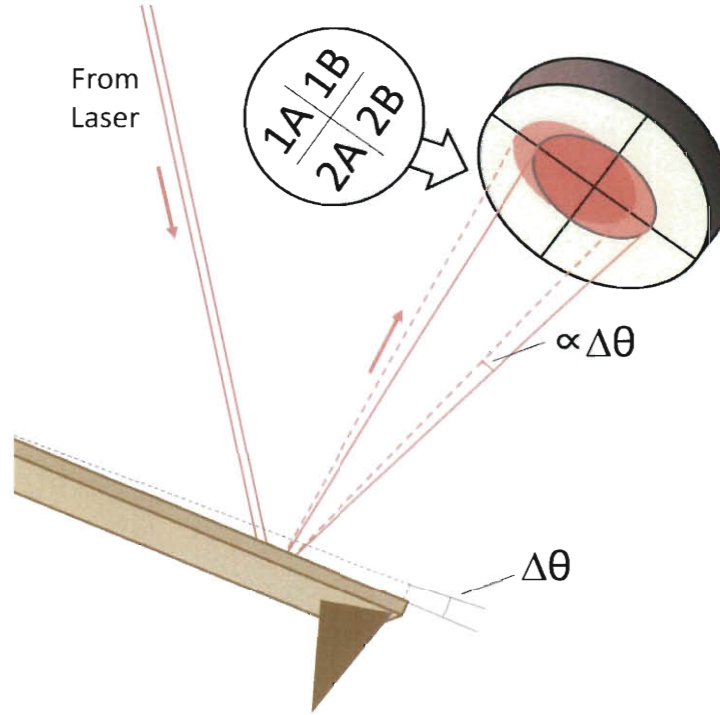
Figure 1.2: Illustration of changes observed by the segmented photodetector as a deflection at the probe tip increases its slope by $\Delta\theta$. Quadrants $1A$, $1B$, $2A$, $2B$ are ordered as shown.

Through calibration, covered in more detail in Section 2.4.1, probe tip deflection is calculated from this difference signal measured by the photodetector. Accurate measurement capability therefore depends on maintaining the slope-displacement relationship from calibration. Only lateral displacements are of interest in standard AFM, and therefore only the difference signal between the corresponding $1 - 2$ quadrants is used for displacement calculation. In the preceding example, this difference signal was $0\ Volts$ before the probe was deflected and $7 - 3 = 5\ Volts$ after deflection. Note that Fig. 1.2 is intentionally drawn not-to-scale in order for all components to be presented together. In an actual AFM system the distance between the probe and photodetector would be very large compared with the spot size and probe deflection, and the diameter of the laser beam would essentially remain constant throughout its

path from laser to photodetector.

Since accurate displacement measurement capability relies on maintaining the slope-displacement relationship from calibration, it is important to identify the operation conditions which preserve this relationship. Standard dynamic AFM imaging and manipulation techniques employ excitation near the probe's fundamental frequency to exploit its most significant resonance. At the fundamental frequency, operating away from the influence of surface forces, the response profile consists of only the first mode shape. Because the first mode slope-displacement relationship is preserved, accurate measurement capability is achieved. In the presence of nonlinear surface forces and during off-resonance conditions above the fundamental frequency, however, the influence of higher mode shapes will alter the probe's response profile, changing the slope-displacement relationship and reducing measurement accuracy.

The purpose of the work presented in this thesis is to quantify the accuracy of measurements obtained using the optical lever method as the probe is operated in intermittent contact with a sample under resonant and off-resonant conditions. First, the influence of tip mass, damping and spot position on the slope-displacement relationship under off-resonance free response conditions—where no surface interaction forces are present—are considered. These parameter variations will provide a better understanding of how each factor individually affects the response profile. Intermittent contact feedback control will then be implemented to scan a hard and a soft surface. Changes to the response profile will be monitored as the effective interaction stiffness is changed, corresponding to local surface property variations or tip wear. Measurement accuracy will be calculated from the slope-displacement relationship change at the incident spot position.

1.2   Previous Work

A review of related publications is presented in this section. First, motivation for and applications of off-resonance excitation are examined. Recent studies of the sensitivity and accuracy of the optical lever method are presented next. Finally, measurement error and response changes due to bistability are briefly discussed.

1.2.1   Off-Resonance Excitation

Chin *et al.* (1994) and Thota and Dankowicz (2006) examined bifurcations produced at the point where an oscillator transitions into an impacting state, a condition known as "grazing" [8, 9]. Dick *et al.* (2009) later extended the same theory to tapping-mode AFM systems in order to reduce contact-force magnitude [10]. Qualitative response changes at the grazing boundary are often too small to detect for excitation at the fundamental frequency. However, when operating at two-and-a-half times the fundamental frequency, a period doubling bifurcation corresponding to the grazing condition was easily observed in experiments.

Dick and Huang continued to examine the period doubling bifurcation in 2009, conducting numerical simulations to study its behavior [11]. A relationship between the effective interaction stiffness and nominal separation distance of the period doubling bifurcation was discovered for excitation at two and a half times the fundamental frequency. By identifying the location of the period doubling bifurcation in a soft sample and utilizing this trend, it may be possible to characterize local material stiffness. Due to the unique characteristics and promising applications related to the frequency at two-and-a-half times the fundamental, measurement accuracy at this particular off-resonance frequency is of interest to the research presented in this thesis.

Dick and Solares (2011) expanded this work by considering a dual-frequency excitation consisting of a primary component at the fundamental frequency and a small

off-resonance component at two-and-a-half times the fundamental frequency [12]. Previous studies of dual-frequency excitation in AFM have incorporated the first two modes, demonstrating increased sensitivity and decreased transitions in the bistable region [13, 14]. Whereas the contact force levels required to observe the bifurcation were high when operating at the single off-resonance excitation, the forces were minimized during dual-frequency excitation. Utilizing only the spectral content of the dual-frequency response, Dick and Solares were able to differentiate between the attractive and repulsive response regimes. The results from this study lay the groundwork for a novel AFM operation mode in which the probe could be operated in the attractive regime only, drastically reducing contact force levels. For the measurement accuracy study presented within this thesis, however, the probe response at the fundamental and off-resonance frequencies are studied individually to identify their response characteristics separately.

A number of other studies have demonstrated additional applications and potential benefits of higher frequency excitation. Pfeiffer *et al.* (2000) studied off-resonance response characteristics of a rectangular micro-cantilever in ultra high vacuum [15]. The reduced quality factors resulting from higher frequency excitations allowed the probe to respond faster to tip-sample interaction changes. In 2003, Hoffmann demonstrated direct measurement of force gradients using off resonance excitation below the probe's fundamental frequency [16]. Stark (2004) examined the influence of tip-sample forces on higher mode shapes using state-space models in order to estimate material properties [17].

Arafat, Nayfeh and Abdel-Rahman (2008) studied measurement error in off-resonance AFM due to resonant interactions between the dynamic modes of the probe [18]. Approximate analytical solutions were developed using the method of multiple scales. A significant internal resonance was observed between the second and third modes when the oscillation frequency matched either of these modes. This

internal resonance was demonstrated as one potential source of measurement error when operating at higher harmonics. In contrast, the frequency range studied within this thesis is between the second and third modes, where higher harmonics and non-linear tip sample forces influence changes to the response profile, but below the range of this internal resonance.

1.2.2 Optical Lever Method

One of the largest potential sources for error in both resonant and off-resonance as well as static AFM operation is the optical lever method. While this method has proven to be a powerful and effective element of the AFM system, the indirect manner in which measurements are obtained require a thorough understanding of the interaction between each component. The interaction between the force applied at the probe and the difference signal, and consequently the measurement accuracy, is affected by parameters such as the laser spot size and position, geometry of the laser setup and even the heat introduced by the power of the laser.

Schäffer and Hansma (1998) designed an aperture to enable adjustment of the laser spot size reflected off an AFM probe in order to maximize detection sensitivity [19]. Their work was conducted at a time when the range of probe sizes available for the AFM system was rapidly expanding. New probes as small as $10\mu m$ offered the advantage of a higher natural frequency, but to maximize the signal-to-noise ratio it is crucial to choose an appropriate spot size based on the size of the probe. Through theoretical models and a self-constructed experimental AFM setup, Schäffer and Hansma demonstrated the potential of their aperture, successfully doubling the signal-to-noise ratio.

More detailed investigation of the optimum choice of spot size and location was performed by Stark (2004) and Schäffer and Fuchs (2005). Stark chose an analytical approach, deriving a state space representation of the equations of motion describing

the beam [20]. Probe dynamics, spot shape, distribution of spot intensity, wavelength of the laser beam and optical losses were accounted for in the dynamic model. In order to optimize sensitivity, Stark focused on the interaction between the poles and zeros of the transfer functions. Recommendations were given for spot size and location relative to the frequency of response to be studied.

Expanding on Stark's work, Schäffer and Fuchs conducted a more thorough quantitative numerical analysis of the effect of laser spot size and placement on detection sensitivity [21]. Additional factors considered in the theoretical model included correction to the laser spot distribution relative to geometric factors: cantilever setup, incident beam and scanner angle combined with probe deflection in two dimensions. Sensitivity was quantified as the difference signal received by the photodetector, a more direct representation of actual operation compared to the work of Stark. Recommendations were presented to achieve optimum global and local detection sensitivity relative to the mode number of response to be studied. Additional suggestions were presented when simultaneous detection of multiple normal modes is considered.

In contrast to the previous two publications, a geometry-focused laser detection sensitivity study was conducted by Beaulieu *et al.* in 2007 [22]. Optics equations and vector analysis were implemented to derive an analytical model relating the cantilever deflection and photodetector difference signal. While this work considered the important implications of arbitrary setup angles in all three dimensions, other critical factors from previous works were ignored, namely spot size and distribution. Instead, spot size was considered infinitesimally small, an approximation that may or may not be warranted depending on the equipment used. Spot placement on the cantilever was considered, but generally held near the free end of the probe, consistent with general recommendations given by Schäffer and Fuchs. Guidelines are presented within to either maximize detection sensitivity or linearize the relationship between cantilever deflection and photodetector difference signal, a crucial requirement to en-

sure the greatest accuracy of AFM measurements. Experimental verification showed very close correlation with analytical results.

In 2008, Xie *et al.* proposed a novel calibration method to increase measurement optical lever sensitivity and measurement accuracy in AFM [23]. Common practice in AFM operation is to tune the system to operate within the linear range of the photodetector calibration curve. The nonlinear curve fit proposed by Xie *et al.* was demonstrated to extend the usable range of the photodetector from 36% to 95% of the total voltage output. With a greater voltage range available, the ratio of difference signal to probe displacement increased, improving sensitivity. This nonlinear calibration demonstrates great potential to increase measurement accuracy, but like the common linear calibration, its accuracy relies on the fundamental assumption of a consistent first-mode response profile.

Another less obvious factor to consider in laser based detection is the heat produced by the laser. Yang et al. (2009) investigated property changes introduced by the joule heating of the laser, specifically the shift in the resonant frequency of the AFM cantilever [24]. Correct knowledge of the probe's resonant frequency is important in a number of AFM applications, most notably material property identification techniques such as atomic force acoustic microscopy (AFAM). The authors constructed an experimental setup to observe changes in the response behavior of a set of probes of various sizes. The laser deflection setup was constructed in the lab to simulate a commercial AFM setup, and the test cantilevers were fabricated by the researchers from <110> oriented single crystal silicon. A small frequency shift generally less than 1 kHz was observed for up to a fourfold increase in laser power. The frequency shift from joule heating of the laser was recommended to be considered for high frequency, low damping applications where frequency resolution is critical, such as frequency modulation atomic force microscopy (FM-AFM).

1.2.3 Bistability

A review of factors affecting measurement accuracy would not be complete without the mention of bistability, one of the biggest challenges in modern AFM [4, 25]. Bistability, due to the presence of both attractive and repulsive nonlinear forces at the surface, often results in unpredictable response transitions and image distortion. García and San Paulo (2000) used numerical simulations to study the interaction behavior between the probe tip, modeled as a single-degree-of-freedom oscillator, and surface forces from a DMT force model [26]. By observing the phase portraits of the response, the authors identified the distribution of the low and high amplitude response solutions based on initial conditions and separation distance.

The phase space primarily consists of steady state solutions in the low amplitude regime for large separation distances, and the high amplitude regime for small separation distances. Between these extremes, there is a transition period where the phase space displays equal attraction to each solution type. Within this range, intrinsic perturbations can easily initiate an undesired transition between response regimes. Response transitions resulting from bistability are beyond the scope of this thesis. It is well known that the abrupt transitions associated with bistability introduce measurement error. However, the minimization of this error does not result from studying the response of the probe, but rather by introducing methods to avoid these bistable conditions. Therefore, excitation magnitudes and stiffness parameters in this thesis were selected to minimize bistable transitions.

Chapter 2

Modeling

In this chapter, the numerical model of the AM-AFM system is developed. First, theory from mechanics of materials and dynamics are incorporated to derive the governing equations of motion of the probe. Equations are derived to characterize the base excitation signal and the surface interaction forces. The following section describes how each of the governing equations are implemented to produce the desired output. Additional clarification of the calibration methods and signal processing within the model is discussed.

2.1 Differential Equations of Motion

In order to best account for the complex spatial response of the AFM probe, modal approximation is used to derive the governing differential equations for subsequent numerical analysis. Since the displacement of the probe is generally less than 0.1% of the probe's length, linear behavior can be assumed. By using a modal approximation, the distributed parameter beam with infinite degrees of freedom can be approximated as a finite number of single degree of freedom (DOF) oscillators representing the first N modes of the probe, whose responses can then be superimposed to describe the total probe response.
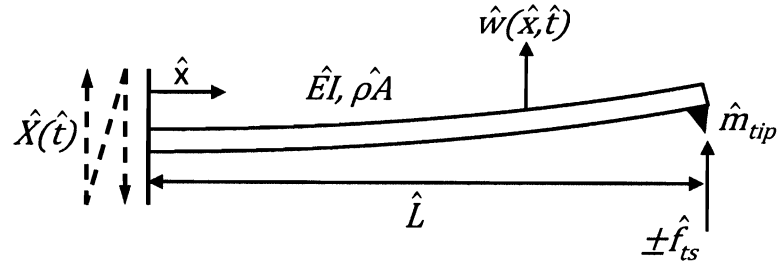
Figure 2.1: Simplified model of a rectangular cantilever probe.

2.1.1 Non-dimensionalization

Derivation of the equations of motion for the AFM probe begins with Euler-Bernoulli equation for a uniform rectangular beam, illustrated in Fig. 2.1. The flexural stiffness is represented by $\hat{E}I$ and mass per unit area by $\hat{\rho A}$. Transverse probe displacement $\hat{w}$ is displayed as a function of distance $\hat{x}$ from the probe base and time $\hat{t}$. Base displacement is denoted by $\hat{X}$ and is employed using a moving reference frame defined by $\widetilde{w}(\hat{x}, \hat{t}) = \hat{w}(\hat{x}, \hat{t}) + \hat{X}(\hat{t})$. The "hat" symbol (ˆ) symbol is used to denote all dimensional quantities. Eqn. (2.1) represents the common form of the Euler-Bernoulli beam equation within a moving reference frame.

$$\hat{E}I \frac{\partial^4 \hat{w}\left(\hat{x}, \hat{t}\right)}{\partial \hat{x}^4} + \hat{\rho A} \frac{\partial^2 \hat{w}\left(\hat{x}, \hat{t}\right)}{\partial \hat{t}^2} = -\hat{\rho A} \frac{d^2 \hat{X}\left(\hat{t}\right)}{d\hat{t}^2}. \tag{2.1}$$

In order to both simplify computation and efficiently account for the extremely small length scale, non-dimensionalization is employed. First, displacement quantities are normalized by $\hat{L}$, the dimensional length of the probe.

$$\hat{x} = x\hat{L}, \tag{2.2}$$

$$\frac{\partial}{\partial \hat{x}} = \frac{1}{\hat{L}} \frac{\partial}{\partial x}, \tag{2.3}$$

$$\hat{w} = w\hat{L}, \tag{2.4}$$

$$\hat{X} = X\hat{L}. \tag{2.5}$$

Equations (2.2 - 2.5) are substituted into (2.1),

$$\frac{\hat{E}I}{\hat{L}^4}\hat{L} \frac{\partial^4 w\left(x, \hat{t}\right)}{\partial x^4} + \rho\hat{A}\hat{L} \frac{\partial^2 w\left(x, \hat{t}\right)}{\partial \hat{t}^2} = -\rho\hat{A}\hat{L} \frac{d^2 X\left(\hat{t}\right)}{d\hat{t}^2}, \tag{2.6}$$

and rearranged to the partial-dimensional form in Eq. (2.7).

$$\frac{\partial^4 w\left(x, \hat{t}\right)}{\partial x^4} + \rho\hat{A} \frac{\hat{L}^4}{\hat{E}I} \frac{\partial^2 w\left(x, \hat{t}\right)}{\partial \hat{t}^2} = -\rho\hat{A} \frac{\hat{L}^4}{\hat{E}I} \frac{d^2 X\left(\hat{t}\right)}{d\hat{t}^2}. \tag{2.7}$$

Next, time is non-dimensionalized, normalizing by the coefficient of the acceleration term,

$$\hat{t} = t\sqrt{\frac{\rho\hat{A}}{\hat{E}I}\hat{L}^4}, \tag{2.8}$$

$$\frac{\partial}{\partial \hat{t}} = \sqrt{\frac{\hat{E}I}{\rho\hat{A}\hat{L}^4}} \frac{\partial}{\partial t}, \tag{2.9}$$

and substituted back into Eq. (2.7) to give the fully non-dimensionalized fourth order differential equation of motion, Eq. (2.10).

$$\frac{\partial^4 w\left(x, t\right)}{\partial x^4} + \frac{\partial^2 w\left(x, t\right)}{\partial t^2} = -\frac{d^2 X\left(t\right)}{dt^2}. \tag{2.10}$$

2.1.2 Discretization

A transformation of the governing fourth order differential equation (2.10) is desired, to return a set of second order ordinary differential equations which can be solved by numerical methods. Separation of variables is employed to express the probe response as a linear combination of mode shapes $\phi_n(x)$ and temporal responses $q_n(t)$ for each mode number n up to order of approximation N, Eq. 2.11.

$$w(x,t) \approx \sum_{n=1}^{N} \phi_n(x) q_n(t), \tag{2.11}$$

or, using the common convention of implicit summation over repeated indices,

$$w(x,t) \approx \phi_n(x) q_n(t). \tag{2.12}$$

Substitution into non-dimensionalized beam equation (2.10) gives,

$$\phi_n''''(x) q_n(t) + \phi_n(x) \ddot{q}_n(t) = -\ddot{X}(t), \tag{2.13}$$

where partial derivatives with respect to space have been replaced with the prime symbol ($'$) and partial derivatives with respect to time with an over-dot ($\dot{\ }$).

A primary goal when implementing separation of variables (2.12) is to use orthogonal mode shapes such that the equations of motion for a multi- or infinite-DOF system can be approximated as a linear combination of the response of N single-DOF oscillators, uncoupled with respect to mass and stiffness. By using the Galerkin Method, we take the inner product of both sides of Eqn. (2.13) with a comparison function, mode shape $\phi_m(x)$,

$$\left(\int_0^1 \phi_m(x)\phi_n''''(x)dx \right) q_n(t) + \left(\int_0^1 \phi_m(x)\phi_n(x)dx \right) \ddot{q}_n(t) \qquad (2.14)$$

$$= -\ddot{X}(t) \int_0^1 \phi_m(x)dx.$$

Integration by parts is employed twice to reduce the order of the first term from four to two,

$$\left(\int_0^1 \phi_m(x)\phi_n''''(x)dx \right) q_n(t) = \qquad (2.15)$$

$$\phi_m(1)\phi_n'''(1)q_n(t) - \phi_m(0)\phi_n'''(0)q_n(t) - \phi_m'(1)\phi_n''(1)q_n(t)$$

$$+ \phi_m'(0)\phi_n''(0)q_n(t) + \left(\int_0^1 \phi_m''(x)\phi_n''(x)dx \right) q_n(t).$$

The first four terms in Eqn. (2.15) are expressed in terms of mode shape values at spatial limits $x = 0$ and $x = 1$. While the mode shape profiles have not yet been defined, generic boundary conditions can be utilized to identify zero terms. Boundary conditions for a clamped-free beam are well documented in literature (e.g. [27]) and are expressed in their dimensional form in Eqns. (2.16–2.19), with additional non-homogeneous terms added to the shear condition to account for the tip mass, base excitation and tip sample force.

$$\hat{\phi}_n(0)\,\hat{q}_n(\hat{t}) = 0, \qquad (2.16)$$

$$\hat{\phi}_n'(0)\,\hat{q}_n(\hat{t}) = 0, \qquad (2.17)$$

$$\hat{E}I\,\hat{\phi}_n''(\hat{L})\,\hat{q}_n(\hat{t}) = 0, \qquad (2.18)$$

$$\hat{E}I\,\hat{\phi}_n'''(\hat{L})\,\hat{q}_n(\hat{t}) = \hat{m}_{tip}\left(\hat{\phi}_n(\hat{L})\,\ddot{\hat{q}}_n(\hat{t}) + \ddot{\hat{X}}(\hat{t}) \right) + \hat{f}_{ts}\left(\hat{w}(\hat{L},\hat{t}) \right). \qquad (2.19)$$

Equations (2.16) and (2.17) impose zero displacement and slope, respectively, relative to the base at the fixed end of the probe. Absence of an internal moment at the free end is ensured by Eqn. (2.18), and Eqn. (2.19) describes the shear force at the free end. In the case of a general clamped-free beam, the right hand side of (2.19) would be zero, indicating zero shear force at the free end. In this case, the internal shear force at the free end is assumed to generally be non-zero, equal to the sum of the inertial force from the mass of the probe tip $\hat{m}_{tip}$ and the nonlinear interaction force between the probe tip and sample surface $\hat{f}_{ts}$.

Following the same procedure as Section 2.1.1, Eqns. (2.2–2.5) and (2.8–2.9) are substituted into Eqns. (2.16–2.19) to return the set of fully non-dimensionalized boundary conditions,

$$\phi_n(0)\, q_n(t) = 0, \tag{2.20}$$

$$\phi'_n(0)\, q_n(t) = 0, \tag{2.21}$$

$$\phi''_n(1)\, q_n(t) = 0, \tag{2.22}$$

$$\phi'''_n(1)\, q_n(t) = \gamma\, \phi_n(1)\, \ddot{q}_n(t) + f_{ts}\Big(w(1,t)\Big), \tag{2.23}$$

where tip mass ratio γ has been included to represent the ratio between tip mass $\hat{m}_{tip}$ and the mass of the beam-like portion of the probe $\hat{\rho}\hat{A}\hat{L}$,

$$\gamma = \frac{\hat{m}_{tip}}{\hat{\rho}\hat{A}\hat{L}}, \tag{2.24}$$

and non-dimensional tip sample force has been introduced, related to its dimensional counterpart by,

$$f_{ts} = \hat{f}_{ts}\frac{\hat{L}^2}{\hat{E}\hat{I}}. \tag{2.25}$$

Combining the Galerkin formulation (2.14) with integration by parts substitution

(2.15) and boundary conditions (2.16–2.19) results in a set of N second order ordinary differential equations with respect to time, taking the form of Eqn. (2.26).

$$\boldsymbol{M}\ddot{Q}(t) + \boldsymbol{C}\dot{Q}(t) + \boldsymbol{K}Q(t) = Z(t). \tag{2.26}$$

Temporal response term $Q(t)$ is an $(N \times 1)$ vector with each term n given by the corresponding modal response $q_n(t)$. Matrices $\boldsymbol{M}$, $\boldsymbol{C}$, and $\boldsymbol{K}$ are $(N \times N)$ square matrices representing the effective mass, damping and stiffness properties of the dynamic system, respectively. Excitation term $Z(t)$ is an $(N \times 1)$ vector containing one inertial force term from base acceleration $\ddot{X}(t)$ and one term from nonlinear tip-sample interaction force $f_{ts}(t)$.

Elements of the modal matrices are presented in Eqns. (2.27–2.29). Equation (2.30) displays the value of each element in the excitation vector. Proportional damping is implemented to account for the low viscous damping of operation in air. Damping terms are defined by a combination the mass and stiffness matrices and dimensionless quality factor Q according to Eqn. (2.28).

$$M_{nm} = \int_0^1 \phi_n(x)\phi_m(x)dx + \gamma\phi_n(1)\phi_m(1), \tag{2.27}$$

$$C_{nm} = \left[\sqrt{\boldsymbol{K}\boldsymbol{M}^{-1}}\right]_{nm}/Q, \tag{2.28}$$

$$K_{nm} = \int_0^1 \phi_n''(x)\phi_m''(x)dx, \tag{2.29}$$

$$Z_n = -\ddot{X}(t)\int_0^1 \phi_n(x)dx - \ddot{X}(t)\phi_n(1) - \phi_n(1)f_{ts}(t). \tag{2.30}$$

Note that the order of the m and n terms have been reversed from their presentation in Eqn. (2.14), taking into account the symmetry of each matrix, and the single index in the excitation vector has been changed from m to n. These modifications have no effect on the meaning of the equations and are applied to maintain labeling

consistency of the rows and columns of each matrix and vector.

2.1.3 Mode Shapes

In order to solve the governing dynamic equations (2.26), characterization of mode shapes is necessary. In other words, the spatial response profile of each mode n must be determined. In order to begin, the temporal response of each mode $q_n(t)$ is approximated by a periodic response with magnitude $q_{0,n}$,

$$q_n(t) = q_{0,n} \, e^{\imath \omega_n t}, \tag{2.31}$$

and substituted into a conservative, unexcited form of the equation of motion (2.13),

$$\phi_n''''(x) \, q_{0,n} \, e^{\imath \omega_n t} - \phi_n(x) \, \omega_n^2 \, q_{0,n} \, e^{\imath \omega_n t} = 0. \tag{2.32}$$

Canceling out like terms returns a fourth order differential equation with respect to spatial variable x only,

$$\phi_n''''(x) - \phi_n(x) \, \omega_n^2 = 0, \tag{2.33}$$

or, substituting

$$\omega_n = \beta_n^2, \tag{2.34}$$

the differential mode shape equation becomes,

$$\phi_n''''(x) - \phi_n(x) \, \beta_n^4 = 0. \tag{2.35}$$

Solutions to differential equations of the form (2.35) have been well studied. The mode shape solution takes the general form of Eqn. (2.36).

$$\varphi_n(x) = A_{1,n} \sin(\beta_n x) + A_{2,n} \cos(\beta_n x) + A_{3,n} \sinh(\beta_n x) + A_{4,n} \cosh(\beta_n x). \quad (2.36)$$

Each mode shape contains five unknown constants $A_{j,n}$, $j = (1,4)$, and β_n. Following standard modal analysis procedure, the characteristic equation is determined,

$$1 + \mathbb{C}^{\mathrm{h}} \left(\mathbb{C} - \gamma \, \beta_n \, \mathbb{S} \right) + \gamma \, \beta_n \, \mathbb{C} \, \mathbb{S}^{\mathrm{h}} = 0, \quad (2.37)$$

where the following shorthand has been employed,

$$\mathbb{S} = \sin(\beta_n), \quad (2.38)$$
$$\mathbb{C} = \cos(\beta_n),$$
$$\mathbb{S}^{\mathrm{h}} = \sinh(\beta_n),$$
$$\mathbb{C}^{\mathrm{h}} = \cosh(\beta_n),$$

The roots of the characteristic equation (2.37) give the values of β_n. An infinite number of solutions exist, but only one β_n value is required for each mode shape and therefore only the first N solutions must be calculated. Once β_n values are derived, coefficients $A_{j,n}$ are determined by calculating the eigenvectors of $\boldsymbol{\Gamma_n}$, the coefficient matrix derived by substituting the mode shape equation into each of the boundary conditions.

Due to the linear dependence of the solutions, each general mode shape $\varphi_n(x)$ can be scaled by a scalar coefficient α_n and still satisfy the governing equation and boundary conditions,

$$\phi_n(x) = \alpha_n \, \varphi_n(x). \quad (2.39)$$

Table 2.1: Modal parameters for dynamic system with no tip mass ($\gamma = 0$).

n	β_n	$A_{1,n}$	$A_{2,n}$	$A_{3,n}$	$A_{4,n}$	α_n
1	1.8751	0.4184	-0.5700	-0.4184	0.5700	1.7543
2	4.6941	-0.5456	0.4954	0.5456	-0.4954	2.0186
3	7.8548	-0.4998	0.5002	0.4998	-0.5002	1.9992

Table 2.2: Modal parameters for dynamic system with tip mass equal to three percent of the beam-like portion of the probe ($\gamma = 0.03$).

n	β_n	$A_{1,n}$	$A_{2,n}$	$A_{3,n}$	$A_{4,n}$	α_n
1	1.8226	0.4187	-0.5698	-0.4187	0.5698	1.7311
2	4.5743	-0.5045	0.4955	0.5045	-0.4955	1.9957
3	7.6698	-0.4998	0.5002	0.4998	-0.5002	1.9804

We therefore impose an additional constraint to normalize the diagonal elements of mass matrix $\boldsymbol{M}$ to unity,

$$\int_0^1 \phi_n(x)\phi_n(x)dx + \gamma\phi_n(1)\phi_n(1) = 1. \tag{2.40}$$

Substituting (2.36) and (2.39) into (2.40) and solving gives normalization constants α_n. At this time the mode shapes are fully characterized, defined by Eqns. (2.36) and (2.39). Tables 2.1 and 2.2 present numerical values for all modal and normalization parameters when tip mass is zero and tip mass of 3% the mass of the beam-like portion of the probe, respectively.

Probe parameter values used for dimensional response calculations are chosen to represent Asylum Research AC240TS, a commercially available AFM probe [28]. The probe's effective density and modulus are 1595 kg/m^3 and 136.3 GPa, respectively. Additional parameter values are presented in Table 2.3. Based on nominal geometry,

Table 2.3: Parameters for AC240TS, Asylum Research, www.asylumresearch.com.

Parameter	Value
Length (μm)	240
Width (μm)	30
Thickness (μm)	2.7
Stiffness (N/m)	2
Fundamental Frequency (kHz)	70

the mass of the probe tip is approximately 3% that of the beam-like portion of the probe, $\gamma = 0.03$.

2.2 External Base Excitation

The applied base motion is simple harmonic, described by,

$$X(t) = X_0 \cos(\omega_{ex} t). \tag{2.41}$$

Within Eqn. (2.41), the magnitude of the excitation is represented by X_0. Excitation frequency ω_{ex} will be varied between the fundamental frequency $\omega_{ex} = \omega_1$ and two-and-a-half times the fundamental frequency, $\omega_{ex} = 2.5 \times \omega_1$.

Differentiating Eqn. (2.41) twice with respect to time returns the expression for base acceleration, for direct implementation into the governing equations of motion.

$$\ddot{X}(t) = -X_0 \omega_{ex}^2 \cos(\omega_{ex} t). \tag{2.42}$$

2.3 Surface Interaction Forces

A number of models are available to characterize the surface interaction forces at the micro- and nano- scale. Depending on the application, the influence of various factors on the interaction force must be considered, foremost the elastic forces resulting from the shape, contact and modulus of the interacting bodies. At the micro-scale, surface forces and adhesive forces can also become dominant. In some cases, plasticity and hysteretic behavior between the loading and unloading curves must be taken into account [29].

A few of the most popular interaction force models are Hertz (1881), Derjaguin-Müller-Toporov (1975), Johnson-Kendall-Roberts (1971), and Maugis (1992). Of these, Hertz provides the most simplistic approximation, approximating the repulsive forces from a deformable elastic sphere (probe tip) pressed into a rigid, flat surface (sample). In most applications the elastic deformation of the surface should not be neglected, but the Hertzian model can provide a sufficient approximation when attractive forces are low and contact forces are high.

The remaining interaction force models include additional attractive force terms resulting from the net intermolecular van der Waals forces within a finite range of the surface. Each interaction model is best suited for different applications. For interactions with low effective stiffness, significant attractive forces and large tip radii, the Johnson-Kendall-Roberts (JKR) method provides the best approximation. JKR theory accounts for hysteretic van der Waals forces within the region of contact [30]. Maugis theory provides an interaction model which transitions between the JKR and Derjaguin-Müller-Toporov (DMT) models [31].

For the opposite case of high effective stiffness, low attractive force and small tip radius, the Derjaguin-Müller-Toporov model is preferred. The DMT model expands upon the Hertzian model by including the influence of van der Waals surface forces from a finite region surrounding the deformed sphere [32]. Tip-sample force $\hat{f}_{ts}$ cal-

culated with the DMT model is presented in Eqns. (2.43) and (2.44). Within the equations, $\hat{R}$ represents the tip radius, $\hat{H}$ the Hamaker constant, and $\hat{d}$ the intermolecular distance. Coefficient $\hat{\beta}$ is defined in terms of tip radius and effective elastic modulus $\hat{E}^*$ between the tip and sample as $(4/3)\hat{E}^*\sqrt{\hat{R}}$.

$$\hat{f}^{ts} = \begin{cases} -\dfrac{\hat{H}R}{6\hat{\sigma}_B^2}, & \hat{\sigma}_B \geq \hat{d}, \\[2ex] -\dfrac{\hat{H}R}{6\hat{d}^2} + \hat{\beta}(\hat{d} - \hat{\sigma}_B)^{3/2}, & \hat{\sigma}_B < \hat{d}, \end{cases} \qquad (2.43)$$

$$\hat{\sigma}_B = \hat{w}(\hat{L}, \hat{t}) + \hat{X}(\hat{t}) + \hat{d} - \left(\frac{\hat{H}R}{6\hat{d}^2\hat{\beta}}\right)^{2/3} + \hat{D}. \qquad (2.44)$$

Within Eqn. (2.44), $\hat{\sigma}_B$ represents the effective separation distance from the sample based on the sum of tip response $\hat{w}(\hat{L}, \hat{t})$, base excitation $\hat{X}(\hat{t})$ and separation distance $\hat{D}$. The form of the equation is chosen such that the interaction force is zero at an effective separation distance of zero.

2.4 Integration of Governing Equations to Simulate AFM Measurement

At this time, all equations have been derived to characterize the system dynamics and describe the applied excitation and interaction forces. In this section, the manner in which the equations are combined to accurately simulate an AFM system will be discussed. Calculation of the calibration curve and control system implementation will be presented in subsections within.

Figure 2.2 illustrates the simulation process developed for this thesis to derive meaningful results from the various inputs. Governing equations are presented within the dashed boundary with arrows depicting their interaction. System inputs, shown outside the dashed boundary, include Q factor, tip mass γ, spot position X_p, exci-
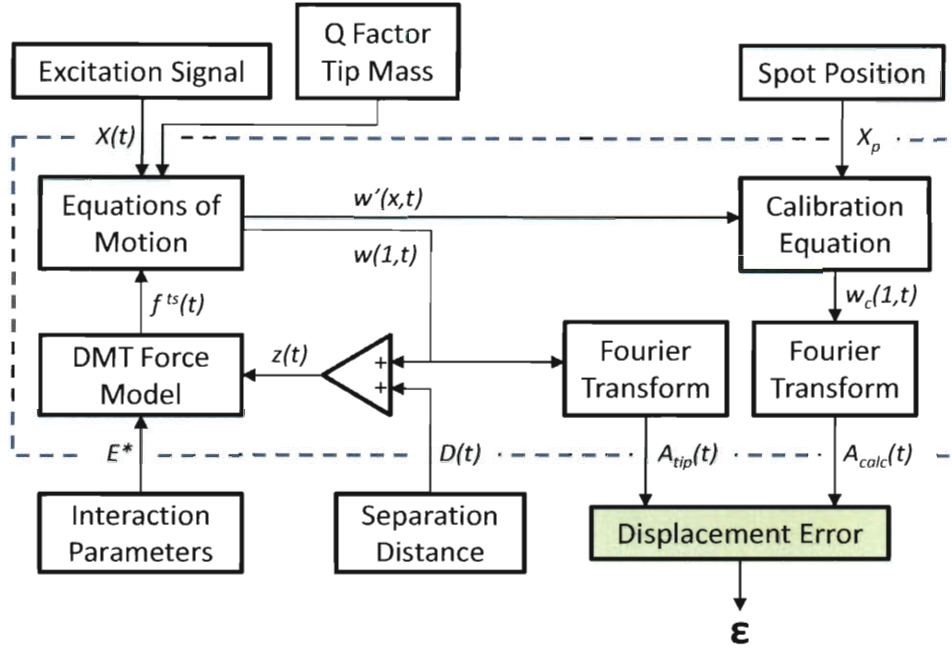
Figure 2.2: Flowchart depicting the interaction between equations and input parameters within the numerical model to calculate displacement measurement error.

tation signal $X(t)$, tip-sample interaction parameters (E^*, H, R, d) and separation distance $D(t)$.

Numerical simulations are performed within the MATLAB environment using a fourth-order Runge-Kutta method. At each time step $t = t_k$, base-relative tip deflection $w(1, t)$ is summed with separation distance $D(t)$, determining the separation distance $z(t)$ between the probe tip and the sample surface. The DMT force model, (2.43–2.44), translates this separation distance into a point force f_{ts}, applied within the equations of motion.

2.4.1 Simulated Calibration

Although the response of the probe $w(x, t)$ is calculated within the dynamic model, real AFM systems lack the ability to directly measure deflection. Recalling Figure 1.1,

the optical lever method calculates tip displacement by measuring a voltage difference signal influenced by the slope of the probe at spot position X_p. Calibration determines the relationship used to calculate tip displacement from this difference signal.

In practice, static calibration is performed by plotting voltage difference signal versus vertical piezo height $D(t)$ while the probe is in contact with a sample surface. Selection of a sample possessing high effective stiffness relative to the cantilever ensures that the vertical piezo height is approximately equal to the tip deflection. A linear curve fit to this data provides the difference signal-deflection relationship used to calculate subsequent measurements.

Since the first mode shape effectively describes the deformation profile produced under the least amount of applied energy, the quasi-static applied tip force applied during calibration leads to the exact same profile. So, the first mode shape and its spatial derivative calculated in Section 2.1.3 provide all information necessary for calibration. The slope-displacement calibration constant C_{sd} is calculated at spot position X_p based on Eqn. 2.45.

$$C_{sd} = \frac{\phi(X_p)}{\phi'(X_p)}. \tag{2.45}$$

Displacement is then calculated within the model as follows,

$$w_c(1,t) = C_{sd}\, w'(X_p, t) \tag{2.46}$$

Two assumptions are made within this optical lever method calibration model. First, the relationship between the slope of the cantilever and the photodetector voltage signal is assumed to be linear. This approximation is made for simplicity and is valid when operating within the linear range of the calibration curve. The focus of this work is on cantilever dynamics which affects the slope-displacement relationship, not the slope-difference signal relationship. A more detailed study of the nonlinearity

of the calibration curve when operating within full detection limits is presented by Xie *et al.* [23].

The laser spot size on the probe is also assumed to be infinitesimally small, deriving displacement from the slope value a single discrete point. The validity of this simplification was tested by comparing difference signals using single-point and finite spot sizes calculated with the relationship presented by Schäffer and Fuchs [21]. The difference signal was effectively identical for spot sizes up to 25% of the probe width when compared with the single-point measurement, so long as the whole spot remained positioned along the probe surface confined within the outer boundaries.

2.4.2 Signal Processing

Separation distance feedback control requires real-time amplitude monitoring of the calculated tip response. In general, the nonlinear tip-sample forces produce an aharmonic response signal, including strong influence from in the frequency band of the primary excitation component as well as varying additional harmonics. A Fourier transform is implemented to extract the amplitude of the response component at the frequency of the primary excitation. Equation (2.47) describes the governing equation from Fourier theory used to derive the amplitude, adapted from reference [33].

$$A_{calc} = \left| \frac{1}{\pi} \int_{t_k-T}^{t_k} w_c(1,t) \, e^{-\imath \omega_{ex} t} \, dt \right|, \quad k = T, 2T, \ldots \tag{2.47}$$

where trapezoidal integration is implemented to approximate the continuous integral in numerical simulations.

Chapter 3

Parametric Analysis for Free Response Conditions

Before studying the behavior under nonlinear interactions with the sample material, a free response case in the absence of surface forces is first considered to examine how spot position, tip mass and quality factor affect optical lever measurements as the spatial response of the probe changes during off resonance excitation. For these simulations, tip-sample force f_{ts} is set to zero and the steady state behavior is studied at different excitation frequencies. The off-resonance excitation introduces predictable changes to the response profile to allow comparison between the influence of spot position, tip mass and quality factor on the slope-displacement relationship. Response amplitude A_{calc} calculated from measured response $w_c(X_p, t)$, Eqns. (2.46) and (2.47), is compared with tip response amplitude A_{tip} calculated from the true response $w(1, t)$ to determine how accurately the optical lever method is measuring tip amplitude. Displacement measurement error ε is then defined as,

$$\varepsilon\,(\%) = \frac{A_{calc} - A_{tip}}{A_{tip}} \times 100.$$

(3.1)

Figure 3.1: Measurement error versus normalized excitation frequency. Curves correspond to results obtained at different spot positions.

3.1 Varying Spot Position

Before intermittent contact is studied in the following chapter, it is important to understand how laser spot position X_p can influence calculated displacement using the optical lever method. Figure 3.1 illustrates measurement error between 0.8 and 2.5 times the fundamental frequency, corresponding to $56 - 175 \ kHz$ based on the dimensional parameters of the probe. The upper limit was chosen to represent the particular frequency where period-doubling behavior has been observed in the work of Dick *et al.* and Dick and Huang [10, 11]. Curves are shown for six discrete laser spot positions from probe midpoint ($X_p = 0.5$) to free end ($X_p = 1.0$). For this initial case, the effect of the tip mass has been removed by setting mass ratio γ equal to zero. Quality factor is fixed at $Q = 50$ to represent reasonable conditions for operation in air.

For excitation at the fundamental frequency ω_1, displacement calculations match exactly for all spot positions. This is exactly as expected, since the response at the fundamental frequency matches the first mode shape, the exact profile of the calibration relationship. For excitation at $2.5 \times \omega_1$, displacement errors range from $\varepsilon = -2\%$ measured at $X_p = 0.5$ to $\varepsilon = +18\%$ measured at $X_p = 1.0$ when compared with the actual amplitude. Measurements obtained at $X_p = 0.52$, accented with circle markers ($\circ$), are determined to accurately predict displacement amplitudes within the frequency range of interest. At this nominal spot position, the slope-displacement relationship has been preserved within the frequency range of interest.

Utilization of this particular spot location where $\varepsilon \approx 0$ could have implications in non-contact AFM or research applications with relatively weak surface interactions where accurate measurement of the tip displacement is necessary. It is of interest to study this point when additional nonlinear forces influence the response behavior to observe whether displacement measurement accuracy is preserved.

3.2   Varying Tip Mass

Mass of the probe tip can vary between commercially available probes based on its unique shape, size and density. The additional mass concentrated on the end of the probe changes the probe's fundamental frequency and response characteristics. Figure 3.2 illustrates the influence of mass ratio on displacement calculations under off resonance excitation. Each curve represents a discrete mass ratio from $\gamma = 0$ to 0.05. Laser spot measurement position is fixed at the free end of the probe, $X_p = 1$, and the quality factor remains at $Q = 50$. The solid curve represents the same set of parameters and is identical to the solid curve in Fig. 3.1. Again, all curves exhibit perfect displacement calulation at the fundamental frequency, when operation conditions match calibration conditions. As excitation levels increase toward $2.5 \times \omega_1$,
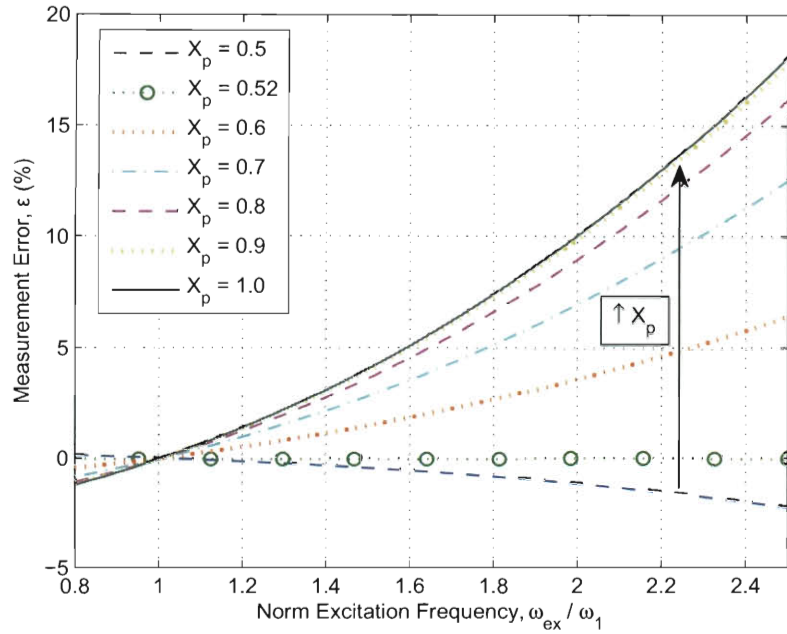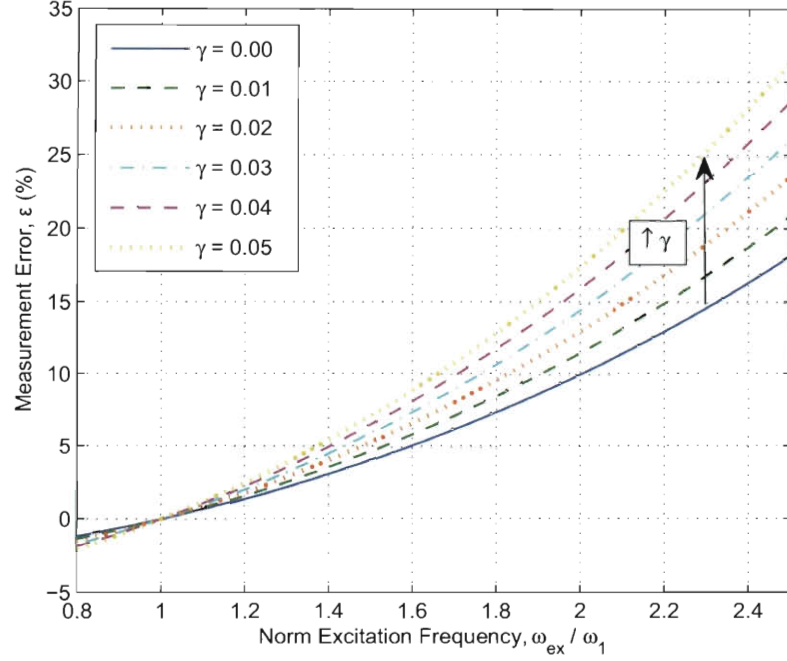
Figure 3.2: Measurement error versus normalized excitation frequency. Curves correspond to results obtained at different tip mass ratios.

response profiles exhibit more drastic change for higher tip mass ratios, leading to larger discrepancies between calculated and actual amplitudes.

These results should be taken into consideration during both equipment selection and operation. For off-resonance applications where accurate displacement measurement is a concern, the probe with the lowest tip mass among those fit to the particular application should be chosen. In applications where a significant amount of material is being added to the tip through contaminants from the surface or intentional bonding, the researcher should expect a corresponding increase in measurement error according to the trend in Fig. 3.2.

Now that the relationship between calculated and actual displacement has been quantified for different X_p and γ, it is helpful to directly examine the profile changes responsible for this behavior. Response profiles and their corresponding slopes are
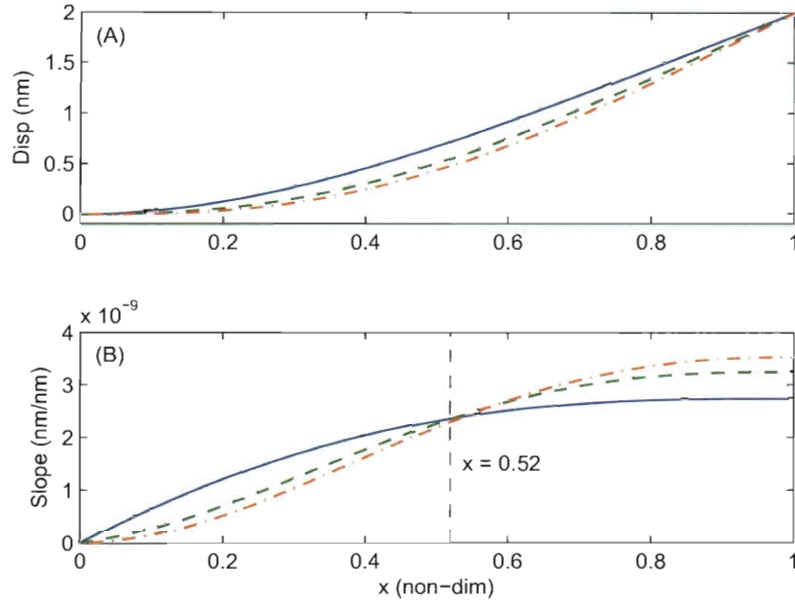
Figure 3.3: Displacement and slope response profiles for $\omega_{ex} = \omega_1$, $\gamma = 0$ (SOLID), $\omega_{ex} = 2.5 \times \omega_1$, $\gamma = 0$ (DASHED) and $\omega_{ex} = 2.5 \times \omega_1$, $\gamma = 0.03$ (DASH-DOT).

compared in Fig. 3.3. Three instances from the results above are illustrated: (1) $\omega_{ex} = \omega_1$, no tip mass, representing the probe's first mode profile from which the static calibration curve is obtained; (2) $\omega_{ex} = 2.5 \times \omega_1$, no tip mass, representing the excitation condition within this study which produces the largest variation of the probe from the fundamental frequency; and (3) $\omega_{ex} = 2.5 \times \omega_1$, $\gamma = 0.03$, including the effect of the mass ratio employed in subsequent intermittent contact simulations. Base excitation amplitudes for each of the three cases are tuned to produce the same response amplitude, in this case 2 nm, for easy comparison. Transverse displacement from a nominal position as a function of non-dimensional position x is presented in Fig. 3.3(A). Response profile differences are clearly seen, but from displacement alone it is difficult to identify the cause of the calculated displacement discrepancies previously discussed. Additional consideration of the slope profile helps clarify the relation to the calibration conditions.

The spot location observed in Fig. 3.1 to maintain perfect measurement capability is most easily identified in Fig. 3.3(B). Slope as a function of non-dimensional position x is presented for each condition. Non-dimensional position $x = 0.52$ is clearly identified as the point where the slope of the off-resonance condition matches the slope at $\omega_{ex} = \omega_1$. In other words, this is the non-dimensional beam position where the slope-displacement relationship from calibration has been preserved.

For applications involving dynamic operation of an AFM probe with negligible influence from surface forces, it would be useful to identify and operate at this spot position. For example, in AFM-based chemical mass detection (e.g. [34]), appropriate spot position selection can help isolate the true response behavior as the chemical mass attaches to the tip. Increased response robustness to the added mass of tip contamination in non-contact AFM is also possible. The increased displacement measurement accuracy should, of course, be weighed against the potential sacrifice in detection sensitivity corresponding to operation much closer to the probe's base. This sensitivity decrease is studied in detail by Stark (2004) and Schäffer and Fuchs (2005) [20, 21].

By examining the modal contributions at off-resonance excitation (Fig. 3.4), a better understanding of the factors governing the location of this ideal spot position can be gained. Panels (A)-(C) display the modal response profiles for $\omega_{ex} = 2.5 \times \omega_1$. Within these panels, the colored curves of various styles correspond to the condition of zero tip mass. The dotted black curves in the same panels correspond to a tip mass of $\gamma = 0.03$. Each modal response has been normalized to a nominal amplitude to clearly illustrate the response profiles. Figure 3.4(D) displays first (DASHED), second (DASH-DOT) and third (SOLID) mode contributions and the resultant response profile (THICK) for $\omega_{ex} = 2.5 \times \omega_1$. It is observed that at this off-resonance frequency of two-and-a-half times the fundamental frequency, the response is still dominated by the first mode, though significant contribution from the second mode is also present.
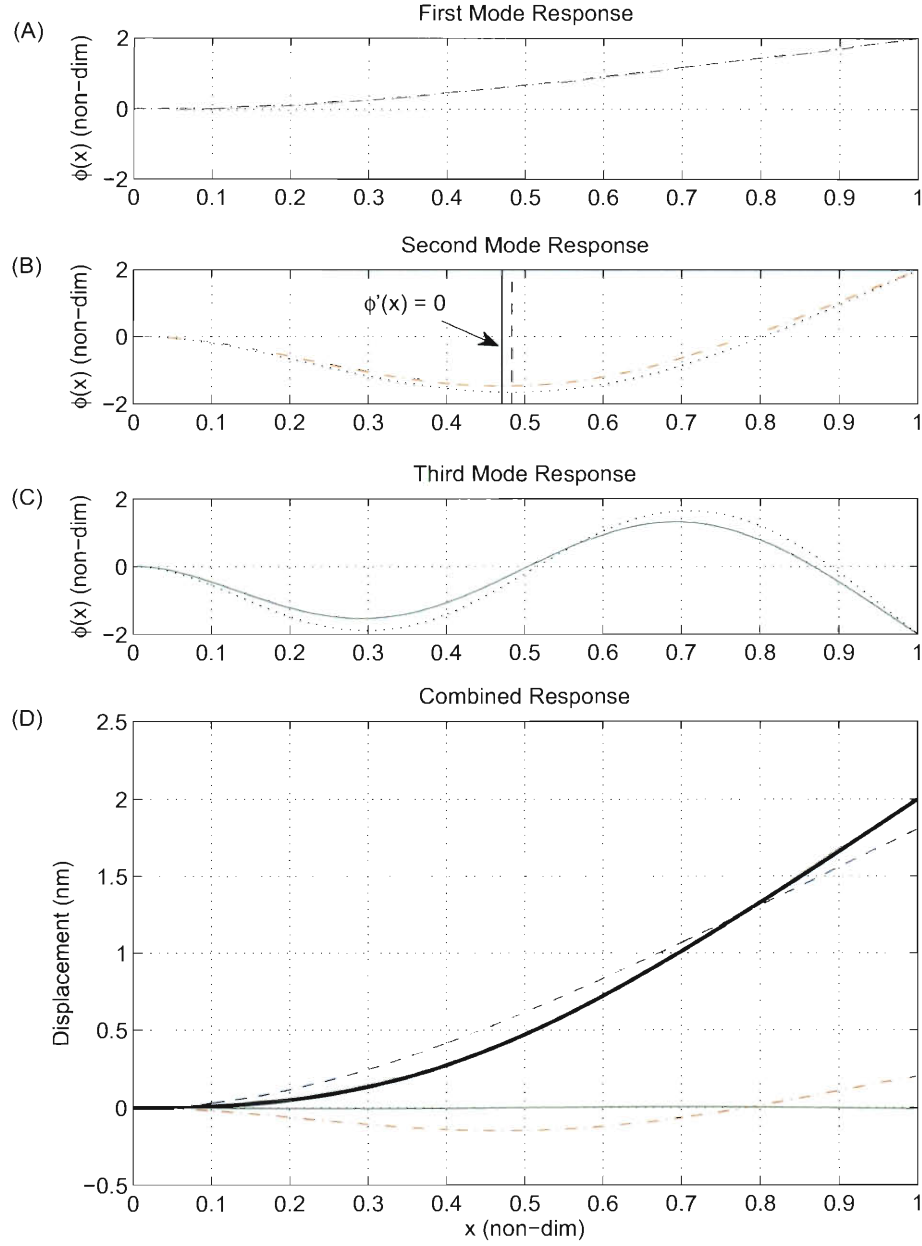
Figure 3.4: Normalized response profiles of the (A) first, (B) second, and (C) third modes for $\omega_{ex} = 2.5 \times \omega_1$, $\gamma = 0$ (COLORED) and $\gamma = 0.03$ (BLACK, DOTTED); (D) modal contributions of the first (DASHED), second (DASH-DOT) and third (SOLID) modes and the resultant response profile (THICK) for $\omega_{ex} = 2.5 \times \omega_1$, $\gamma = 0$.

The third mode exhibits negligible influence in this case.

In Fig. 3.4(B), the anti-node of the second mode response has been identified for zero tip mass (SOLID VERTICAL) and $\gamma = 0.03$ (DASHED VERTICAL). At this location on the probe, influence from the second mode neither adds to nor subtracts from the slope of the first mode profile. However, the positive influence from this mode increases the displacement at the tip and consequently decreases the ratio between slope and displacement from the calibrated relationship. The ideal spot position therefore lies just to the right of this anti-node at the location where a sufficient increase to the slope has been contributed by the second mode to compensate for the increased tip deflection.

3.3   Varying Quality Factor

Quality factor varies between dynamic AFM operation in ultra high vacuum (UHV) and ambient conditions. Figure 3.5 illustrates the influence of the quality factor on displacement measurements for off-resonance conditions. Measurement discrepancy is displayed as the value of the quality factor is varied from $Q = 1 - 10$. Four curves are shown, each representing excitation frequencies from 1.0 to 2.5 $\times \omega_{ex}$. The mass ratio is set at $\gamma = 0$, corresponding to zero tip mass.

In the range between $Q = 2 - 10$, the change in quality factor creates only about 2% change in measurement error at $\omega_{ex} = 2.5 \times \omega_1$ and has even less effect on all other off-resonance frequencies. The only significant change in measurement error appears between $Q = 1 - 2$, corresponding to extremely high levels of damping. Measurement error remains constant as quality factor is increased above $Q = 10$ (not shown). Quality factor for AFM operation in both air and UHV falls well above $Q = 10$ where the response is not sensitive to variations in the quality factor. These results instill confidence that an approximate quality factor of $Q = 50$ can be used without the
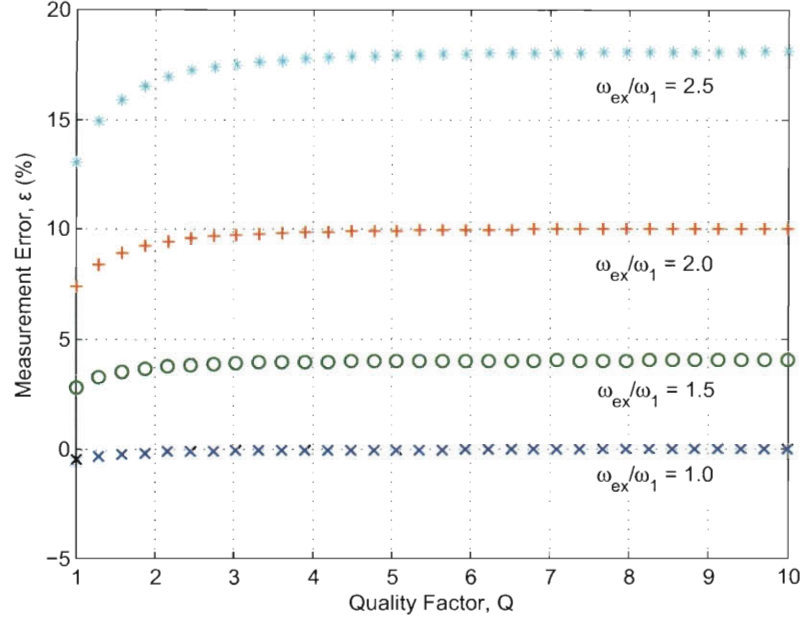
Figure 3.5: Measurement error versus quality factor at nominal excitation frequencies $\omega_{ex}/\omega_1 = 1.0$ ($\times$), $\omega_{ex}/\omega_1 = 1.5$ ($\circ$), $\omega_{ex}/\omega_1 = 2.0$ ($+$) and $\omega_{ex}/\omega_1 = 2.5$ ($*$).

results of the simulation being specific to that parameter choice.

3.4   Combined Influence of Parameters

In order to provide more insight into the coupled influence of mass ratio, spot position and damping on displacement measurements, simulations are conducted for each of the three possible pairs of parameters X_p, γ and Q between the limits defined in Sections 3.1–3.3 for each parameter. All simulations are conducted at the highest excitation frequency considered within this study, $2.5 \times \omega_1$, to observe the largest error magnitudes.

Figure 3.6 displays a contour plot of measured displacement error versus mass ratio and spot position. Each hue represents a error percentage, illustrated by the corresponding color bar. Mass ratio and laser spot position are varied from $\gamma = 0 -$

0.10 and $X_p = 0.5 - 1$, respectively. The white band appearing between $X_p = 0.5 - 0.6$ represents the closest correlation between calculated and actual displacement. The dashed curve in the center of the band identifies the nominal position along the probe where the slope-displacement relationship from calibration is maintained at the off-resonance condition for each mass ratio. It is observed that the exact location of this particular spot position varies slightly with mass ratio, due to a difference in off-resonance response profiles corresponding to variations in tip mass. A similar contour plot with excitation at the fundamental frequency would simply indicate perfect measurement capability for all spot positions and mass ratios, since operation conditions would match calibration conditions.

Whereas measurement error appears highly sensitive to changes in tip mass when the laser spot position is focused at the free end of the probe, as determined in Section 3.2, spot positions focused near the probe midpoint exhibit a much smaller measurement error fluctuation ($\Delta\epsilon < 10\%$) over the same range of mass ratios. This suggests that a system using a laser spot measurement focused near the midpoint will exhibit less measurement error regardless of tip mass than the same measurements taken elsewhere along the probe. Using Fig. 3.6, a spot position can be selected *a priori* based on tip mass, that will accurately measure displacement for off-resonance excitation up to $2.5 \times \omega_1$.

Figure 3.7 displays a contour plot of measurement error versus spot position and quality factor. Measurement error versus tip mass and quality factor is illustrated in Fig. 3.8. These two plots verify the conclusions drawn from Fig. 3.5; namely, for $Q > 3$, measurement error does not vary with quality factor. Only below $Q = 3$ (much higher damping than would be experienced in air) does the measurement error exhibit variation with Q. Both figures confirm that the subsequent results obtained within this study, using a value of $Q = 50$, will not be unique to this particular value of damping.
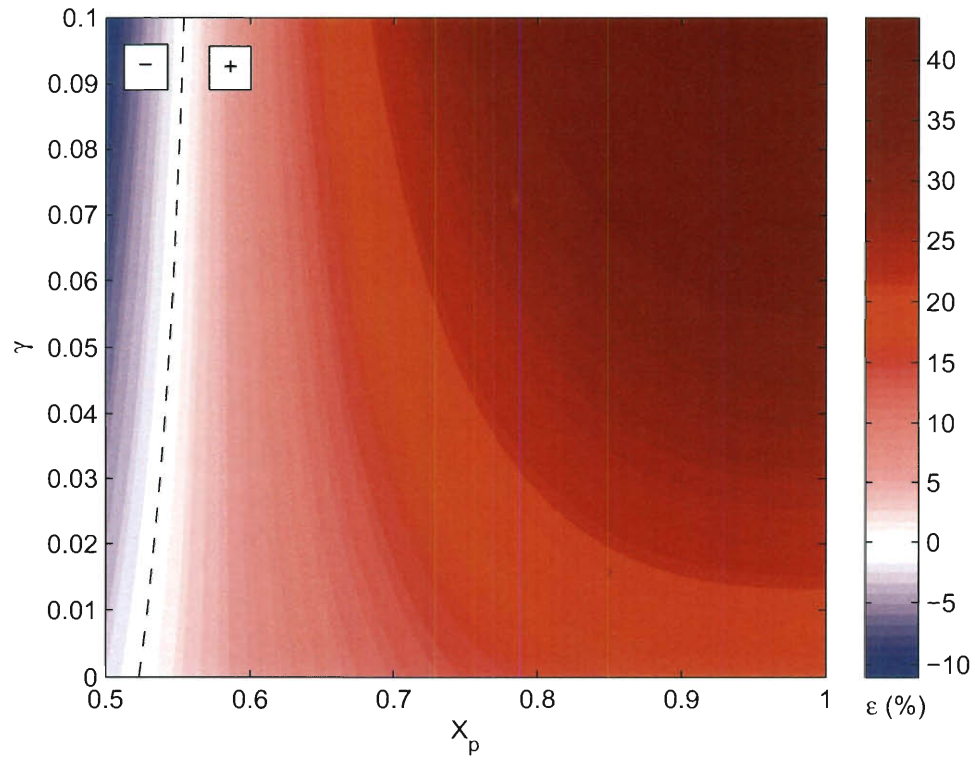
Figure 3.6: Contour plot of measurement error versus mass ratio and spot position for excitation at $2.5 \times \omega_1$. Trend line (DASHED) represents the spot position where $\varepsilon = 0$ at each tip mass. Labels identify positive and negative measurement error regions for grayscale prints.
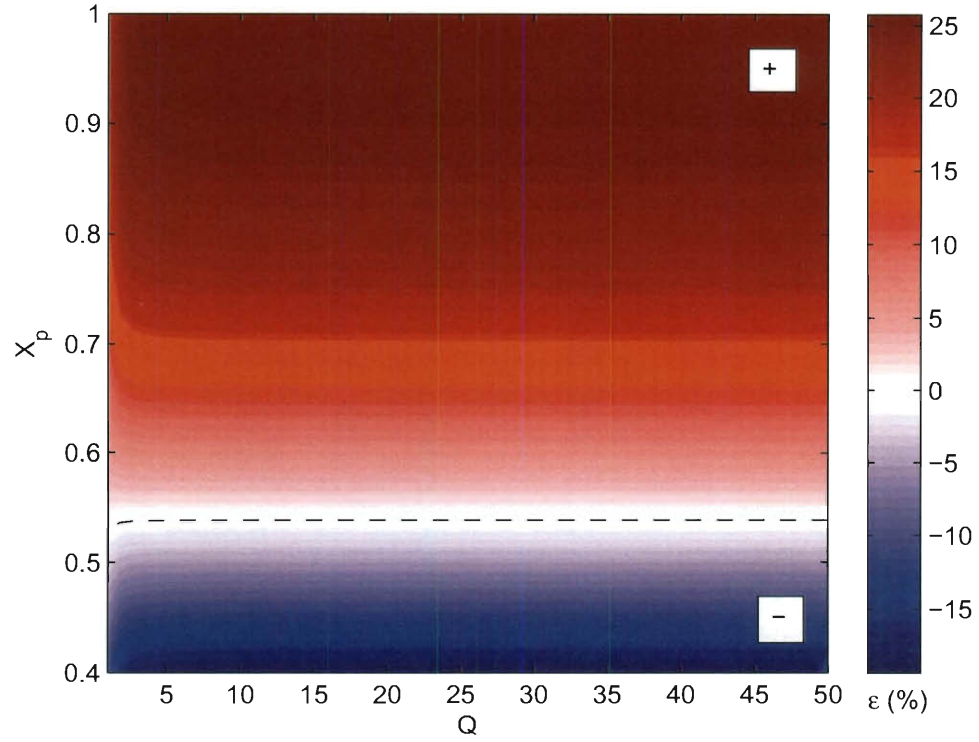
Figure 3.7: Contour plot of measurement error versus spot position and quality factor for $\omega_{ex} = 2.5 \times \omega_1$, $\gamma = 0$. Trend line (DASHED) represents the spot position where $\varepsilon = 0$ at each quality factor. Labels identify positive and negative measurement error regions for grayscale prints.
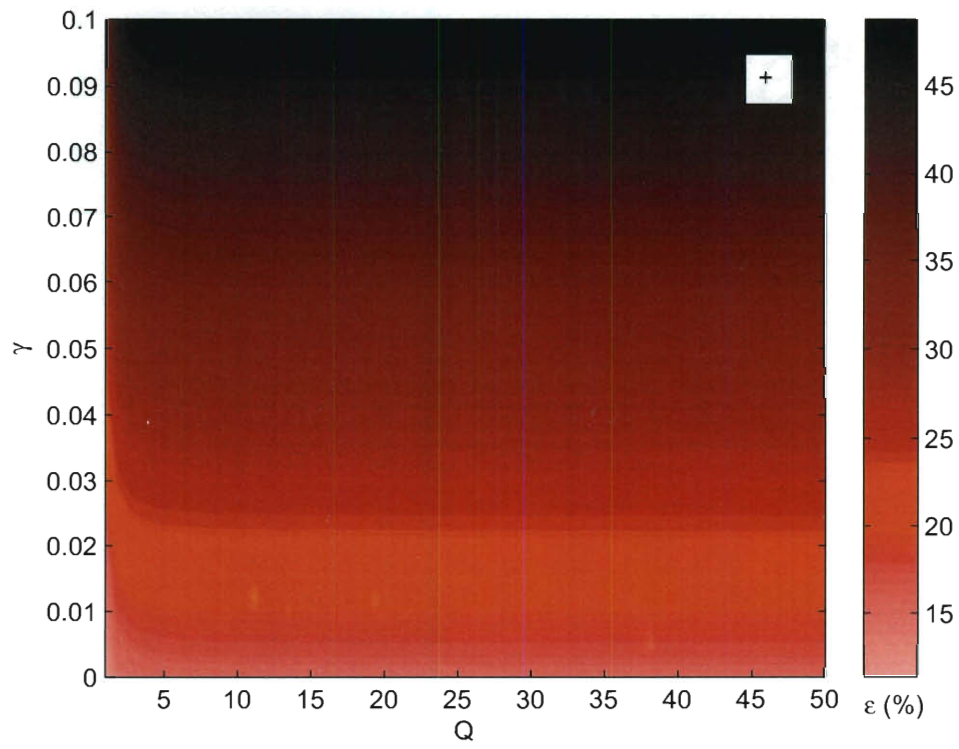
Figure 3.8: Contour plot of measurement error versus tip mass and quality factor for $\omega_{ex} = 2.5 \times \omega_1$, $X_p = 1.0$.

Chapter 4

Results and Analysis for Intermittent Contact Operation

In this section, numerical results are presented to study the response behavior and corresponding measurement accuracy during intermittent contact with the sample surface. As described in Section 2.3, a DMT force model is chosen to define the tip-sample interaction forces near the sample surface. Two sets of force parameters are implemented, listed in Table 4.1. The corresponding materials, silicone rubber and glass, represent a soft and a stiff interaction surface, respectively. First, the force curves will be characterized and changes due to effective modulus variation will be illustrated. Next, measurement accuracy will be determined using a PID control system to measure each of the surfaces as the effective modulus is varied. Finally, a general study of calculated versus true response amplitude will be conducted for off-resonance conditions, from which measurement accuracy can be estimated.

4.1 Interaction Force Curves

Figures 4.1 and 4.2 illustrate the force interaction curves for the silicone rubber and glass surfaces, respectively, as their effective modulus E^* is increased to five and

Table 4.1: Interaction force parameters for intermittent contact simulations

	Silicone Rubber	Glass
Hamaker constant, $\hat{H}$ (Nm)	4.5×10^{-20}	6.6×10^{-20}
Radius, $\hat{R}$ (m)	10×10^{-9}	10×10^{-9}
Intermolecular distance, $\hat{d}$ (m)	0.165×10^{-9}	0.170×10^{-9}
Effective modulus, $\hat{E}^*$ (GPa)	4.50×10^{-3}	4.50×10^{-3}

ten times its original value. In each, the solid line represents the effective stiffness corresponding to the original material. Note the wide variation in scales between the two plots. The change in effective modulus induces drastic changes over a short distance for the hard glass sample, increasing interaction forces from around 10 nN to 100 nN at a penetration of only a tenth of a nanometer into the sample. The most prominent change observed in the silicone rubber sample is a shift in the force threshold, the distance between the initial force interaction most distant from the surface and the zero-force crossing of the force (identified as the surface boundary). The movement of this force threshold is identified with an arrow in Fig. 4.1.

4.2 Measurement Accuracy at the Fundamental Frequency Using PID Control

4.2.1 Controller Description

Feedback control is an essential part of nearly all AFM operation modes. In AM-AFM, a proportional-integral-derivative (PID) controller is implemented to maintain a constant response amplitude by adjusting base separation distance $D(t)$. Equation (4.1) describes the control equation, adapted from Eaton and West [7].
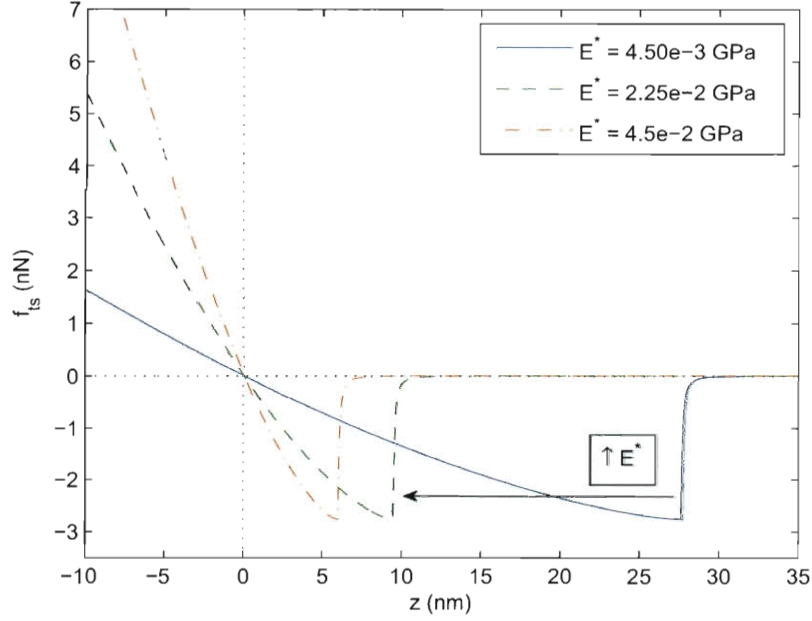
Figure 4.1: Tip-sample interaction force curve for Si probe on silicone rubber, curves plotted for effective modulus values of 1 (SOLID), 5 (DASHED) and 10 (DASH-DOT) times the nominal value.

$$D(t) = C_P \times A_{err}(t) + C_I \times \int A_{err}(t)\, dt + C_D \times \frac{dA_{err}(t)}{dt} \qquad (4.1)$$

Distance adjustments are implemented with the controller at time step $t = t_k$ once every period of oscillation ($k = T, 2T, \dots$). Constants C_P, C_I and C_D are the proportional, integral and derivative control parameters, respectively. The derivative control parameter is set to zero, but the controller will still be referred to by its full title, "PID", following common convention for AFM. The two remaining parameters are tuned to produce desired tracking according to recommendations by Eaton and West (2010). A detailed discussion of the implementation of the controller is discussed in the following section.
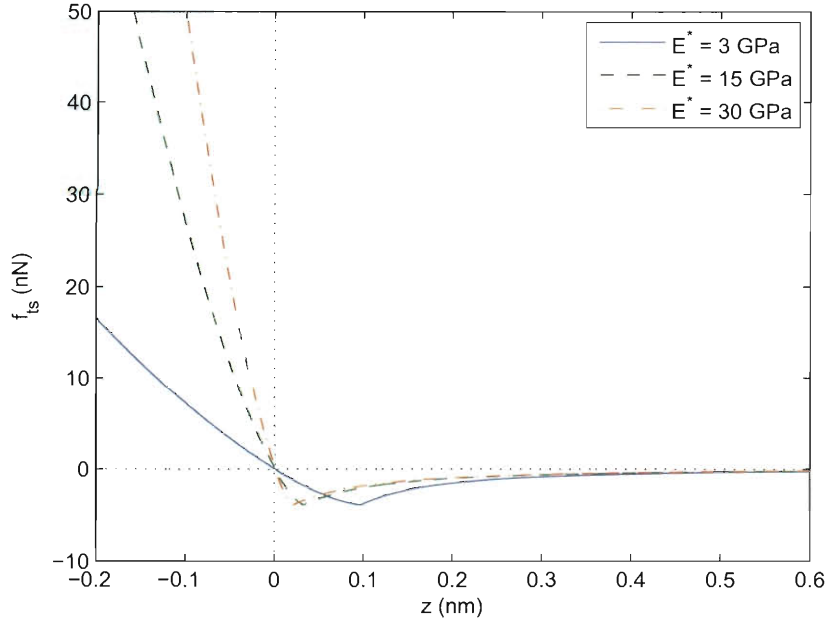
Figure 4.2: Tip-sample interaction force curve for Si probe on glass, curves plotted for effective modulus values of 1 (SOLID), 5 (DASHED) and 10 (DASH-DOT) times the nominal value.

4.2.2 Controller Implementation

Figure 4.3 illustrates how feedback control is implemented within the numerical model to simulate AM-AFM operation. New elements and parameters not implemented in the original numerical model (Fig. 2.2) are shaded. Whereas separation distance $D(t)$ was explicitly defined as a system input in the previous model, $D(t)$ is now calculated within the PID controller from the difference between the calculated amplitude A_{calc} and a user-defined set point amplitude A_{set} according to Eqn. (4.1). Tip-sample separation distance $z(t)$ is also influenced by an additional system input, surface profile S, expressed as a function of position coordinates x_s and y_s in the horizontal plane of the sample. This input is included to simulate changing topography and is used primarily to tune the control parameters by monitoring the probe's response to a stepped surface.
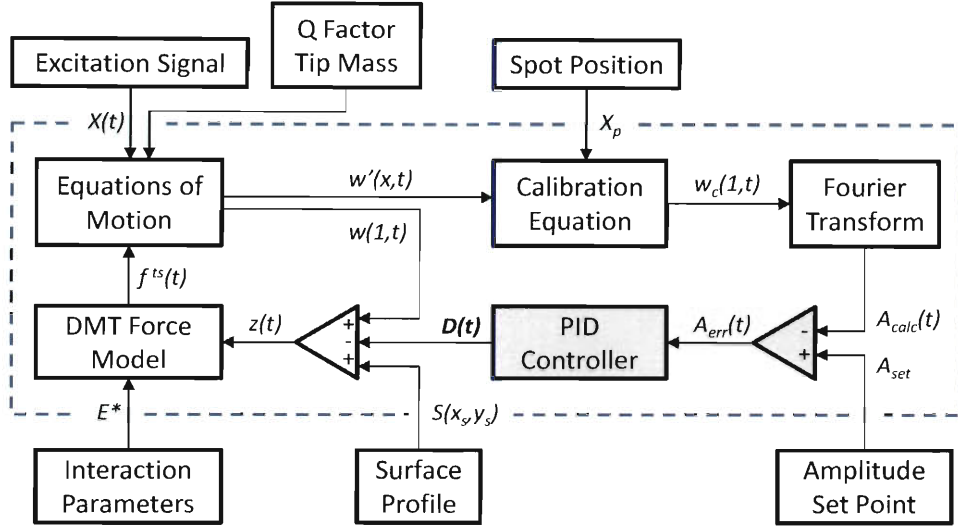
Figure 4.3: Flowchart depicting the interaction between equations and input parameters within the numerical model for feedback control simulations.

Tapping-mode AFM operation at the fundamental frequency will be considered first. Consistent with standard AM-AFM operation, a PID controller is implemented to adjust the vertical separation distance D based on observation of the difference between the set point amplitude and the response amplitude measured with the optical lever method. In order to begin the surface scan, lateral motion is kept stationary and the controller is activated. With the probe starting from a steady state oscillation at 20 nm above the influence of surface forces, the controller brings the probe into intermittent contact with the surface, adjusting the separation distance until the set point amplitude A_{set} is reached. The measured separation distance at this starting point is stored as the reference separation distance D_{ref}, and all height measurements during the scan are expressed in reference to this point.

If the surface topography changes, a corresponding change in response amplitude occurs, at which point the feedback controller adjusts the separation distance to maintain a response amplitude equal to the set point. Under ideal conditions, the

separation distance history provides a perfect representation of the vertical profile of the surface feature. An image of the surface is created by mapping separation distance D versus the lateral (x_s, y_s) surface position.

As the results from Chapter 3 demonstrate, the calculated displacement using the optical lever method can be higher or lower than the actual response amplitude depending on how close the response profile matches the fundamental mode shape. In tapping-mode AFM, if the optical lever method is accurately calculating the true displacement when the reference distance D_{ref} is set, and the displacement calculations remain accurate throughout the scan, clearly the vertical measurement accuracy will be ideal. In the same manner, if the response amplitude calculated with the optical lever method differs from the true response amplitude due to higher mode response from the surface interactions *but* the difference between calculated and true amplitudes is consistent throughout the scan, the vertical measurement accuracy will also be ideal. If, however, the calculated response amplitude is within a certain degree of the true response value at the beginning of the scan and the response profile changes during the scan, the relationship between calculated response amplitude and true response amplitude will also change, and the vertical measurement accuracy will be affected.

Effective modulus variations possess the greatest potential to change the response profile during the scan and therefore are the focus of this chapter. The simulated AM-AFM scanning method described above is implemented to image an atomically flat surface as the effective modulus changes from the nominal value (corresponding to the original E^* value for each material from Table 4.1) to ten times the nominal value. An atomically flat surface is chosen to avoid any influence from transient behavior while scanning varying topography. Hereafter, when referring to the effective modulus in a simulation as E^*_{glass} or E^*_{rubber}, it is implied that the corresponding parameters $\hat{H}$, $\hat{R}$ and $\hat{d}$ from Table 4.1 are also implemented.

Effective modulus changes during operation can be due, for example, to localized material properties or tip wear. Biological specimens exhibit a range of modulus values depending on their composition, from soft membranes to hard protein surfaces [35]. Lin, Dimitriadis and Horkay (2007) observed effective modulus fluctuations up to 2000 percent during indentation tests of tissue-engineered cartilage [36]. Tip wear is an inevitable reality in AFM (see, e.g. [37, 38]), leading to increased effective stiffness from the larger interaction area, in addition to the loss of lateral resolution.

4.2.3 Controlled AM-AFM Results

Figures 4.4 and 4.5 display vertical measurement error for the glass and silicone rubber surface, respectively. Since the actual surface is flat ($S(x_s, y_s) = 0$), the measurement error is simply the vertical profile measured during the scan relative to the reference distance D_{ref}. For each case, the width of the imaged area is defined as 50 nm and the lateral scanning speed is held constant at 2500 nm/s. The influence of scanning speed was observed during a number of model verification simulations and was determined to not significantly influence the results.

Measurement error from six separate scans are plotted in Fig. 4.4. The feedback within each scan is controlled by measurements at different spot positions, ranging from the midpoint of the probe, $X_p = 0.5$ to the free end of the probe, $X_p = 1.0$. Base excitation magnitude is tuned to produce a free response amplitude of 20 nm and the set point amplitude is fixed at 18 nm, 90% of the free response, modeling common conditions [7]. Although the effective modulus is steadily increased throughout the scan to a final value 10 times greater, results from scans utilizing each spot position accurately measured the flat surface within 1 nm. Local fluctuations observed in the measurement profile of each are likely due to the control system over- or under-correcting on the subnanometer scale.

Figure 4.5 illustrates measurement error for scans utilizing six different spot posi-

Figure 4.4: Vertical measurement error during a simulated tapping-mode scan of a 50 nm flat glass surface. Curves represent simulations conducted utilizing different spot positions $X_p = 0.5 - 1.0$.

tions on a flat silicone rubber surface as the effective modulus is increased by 10 times its nominal value. Curves from all six scans overlay one another, indicating that the exact same response is observed at each of the spot positions, causing the controller to respond the same in each scan and produce identical error curves. Plotted alongside the curves are markers ($\times$) representing the shift of the force threshold value (see Fig. 4.1). It is observed that the measured error and the force threshold shift follow one another closely as the effective modulus is increased. It is therefore concluded that this measurement error is due to the relocation of the threshold at which the attractive force first acts within the model, and not to a change in response profile. A change of coordinates within the force model—defining the zero surface of the sample as the threshold of the attractive regime—instead calculates sub-nanometer vertical
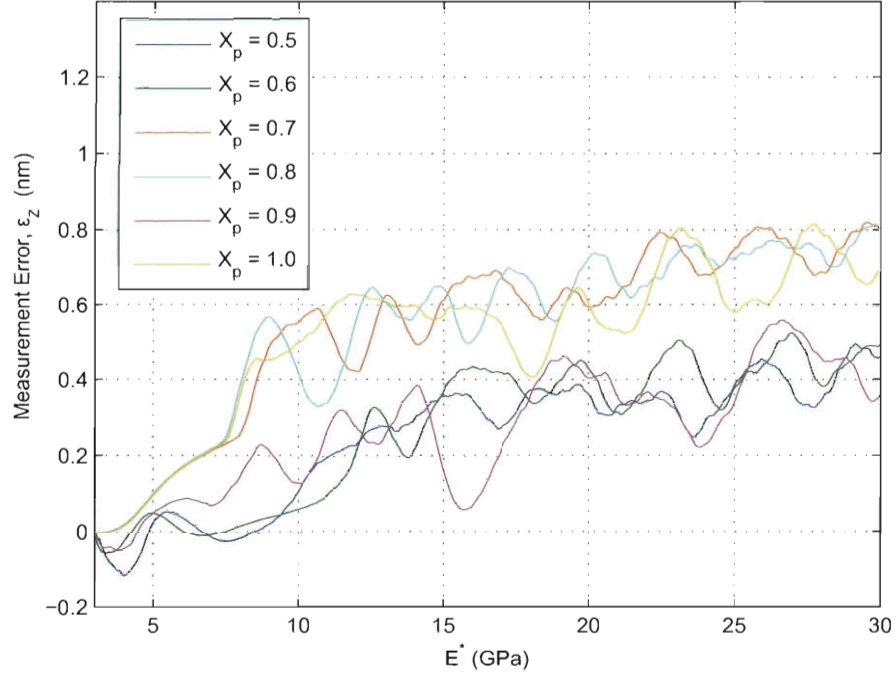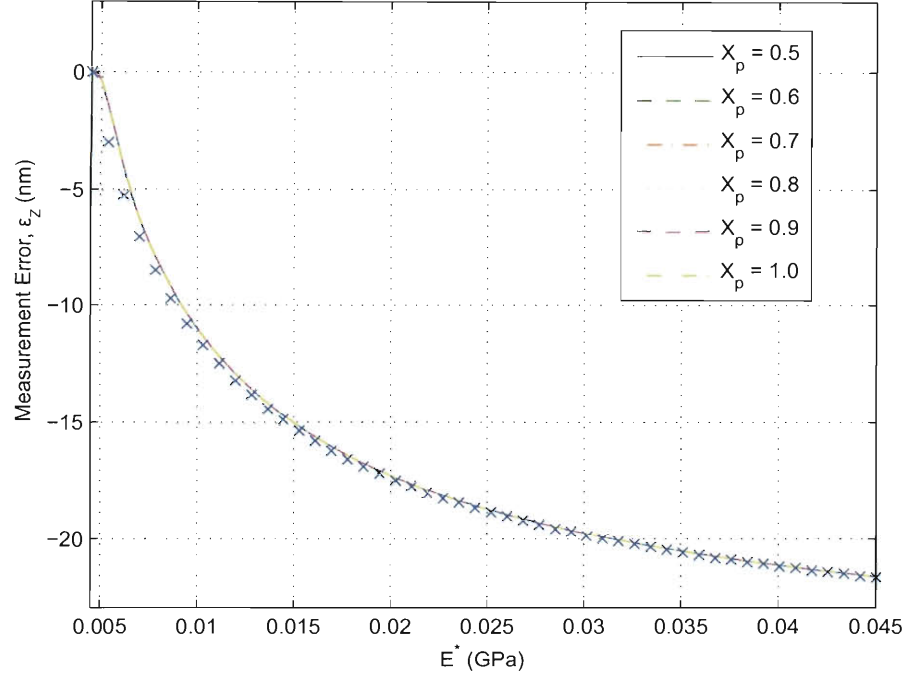
Figure 4.5: Vertical measurement error during a simulated tapping-mode scan of a 50 nm flat silicone rubber surface. Curves represent simulations conducted utilizing different spot positions $X_p = 0.5 - 1.0$ (SOLID); markers ($\times$) represent the movement of the force threshold value.

measurement error for the same simulation.

This conclusion is supported by the perfect correlation between the results at each spot position. A response profile change would be identified by divergence of one or more of the curves, likely all six, signifying that the spatial relationship between the points had changed. It is not overlooked that the force curve for the glass sample exhibits the same threshold movement with increasing stiffness, but it is noted that the total movement is less than one tenth of a nanometer for a $10\times$ increase in stiffness and is determined to be negligible.

From the controlled tapping mode simulations, it is concluded that the response behavior for intermittent contact at the fundamental frequency is consistent through

effective modulus changes in both soft and hard samples, introducing error on the order of less than one nanometer and further confirming its robustness as a powerful imaging tool. Furthermore, the choice of spot position under these conditions does not significantly influence the vertical measurement accuracy, although other implications (e.g. detection sensitivity) regarding choice of spot position are certainly not refuted. In order to account for possible variations based on response amplitude or set point, additional simulations were conducted, implementing free response amplitudes between $5 - 100 \ nm$ and set points between $50\% - 90\%$ of the free response amplitudes. All additional simulations support the original conclusions.

4.3 Off-Resonance Tapping-Mode Response and Accuracy

In order to extend the study to include off-resonance excitation while maintaining the most broad scope of applicability in research, the PID control system is abandoned in subsequent simulations and replaced with a separation distance sweep. As discussed in Section 1.2, current applications of off-resonance excitation are diverse, so it is desired to present the following results in a general sense from which measurement accuracy can be inferred depending on application. First, the measured response at various spot positions will be compared with the actual response amplitude at a range of separation distances for the glass and the silicone rubber sample. Next, a method will be described to estimate vertical measurement error from these response amplitude plots. Finally, displacement measurement error and the existance of the "ideal" spot position will be examined for intermittent contact conditions.

4.3.1 Response Amplitude Versus Separation Distance on Glass Sample

Figures 4.6–4.9 illustrate the measured response as a function of spot position and separation distance as the probe is brought into intermittent contact with a glass surface at an excitation frequency of $\omega_{ex} = 1\times$, $1.5\times$, $2\times$, and $2.5 \times \omega_1$. In all simulations, the magnitude of base excitation is tuned to produce a 20 nm response amplitude. Steady-state conditions are achieved at a separation distance of 25 nm, an initial separation sufficiently far from the attractive regime. Then, the response is observed as separation distance is decreased at a constant rate. A decrease of 0.1 nm per period of oscillation was determined to minimize the effect of transient oscillations. The entire response profile is recorded throughout each simulation, and through post-processing the response amplitudes at the range of spot positions between $X_p = 0.5 - 1.0$ are calculated using the same procedure as the controlled simulations.

Four panels are presented within each figure. Panels (A) and (B) correspond to a simulation at original force parameters of the glass sample. A separate simulation at 10 times the effective modulus for the glass sample is illustrated in (C) and (D). Panels (A) and (C) display the time response signal of the tip over the entire simulation (DOTTED) and the response amplitude calculated from the actual tip response and Eqn. (2.47) (THICK). Panels (B) and (D) are contour plots which use shading to represent calculated response amplitude versus spot position and separation distance. Shading is applied such that a white hue represents the original free response amplitude of 20 nm, red represents values greater and blue, values below. The shading convention is not meant to directly infer accurate measurement, it is only chosen as a reference. Estimating measurement accuracy from the figures will be discussed in more detail after they are presented. Note that axes and colorbar scaling are adjusted in each case to account for both large and small response amplitudes.

Figure 4.6, operating at the fundamental frequency, exhibits consistent response

Figure 4.6: (A) Time response (DOTTED) and corresponding amplitude (THICK) and (B) calculated tip amplitude (SHADED) versus spot position and separation distance for $\omega_{ex} = \omega_1$, $A_{free} = 20\ nm$, and $E^* = E^*_{glass}$; (C) and (D) provide similar illustrations for $E^* = 10 \times E^*_{glass}$.

Figure 4.7: (A) Time response (DOTTED) and corresponding amplitude (THICK) and (B) calculated tip amplitude (SHADED) versus spot position and separation distance for $\omega_{ex} = 1.5 \times \omega_1$, $A_{free} = 20\ nm$, and $E^* = E^*_{glass}$; (C) and (D) provide similar illustrations for $E^* = 10 \times E^*_{glass}$.

Figure 4.8: (A) Time response (DOTTED) and corresponding amplitude (THICK) and (B) calculated tip amplitude (SHADED) versus spot position and separation distance for $\omega_{ex} = 2 \times \omega_1$, $A_{free} = 20\ nm$, and $E^* = E^*_{glass}$; (C) and (D) provide similar illustrations for $E^* = 10 \times E^*_{glass}$.
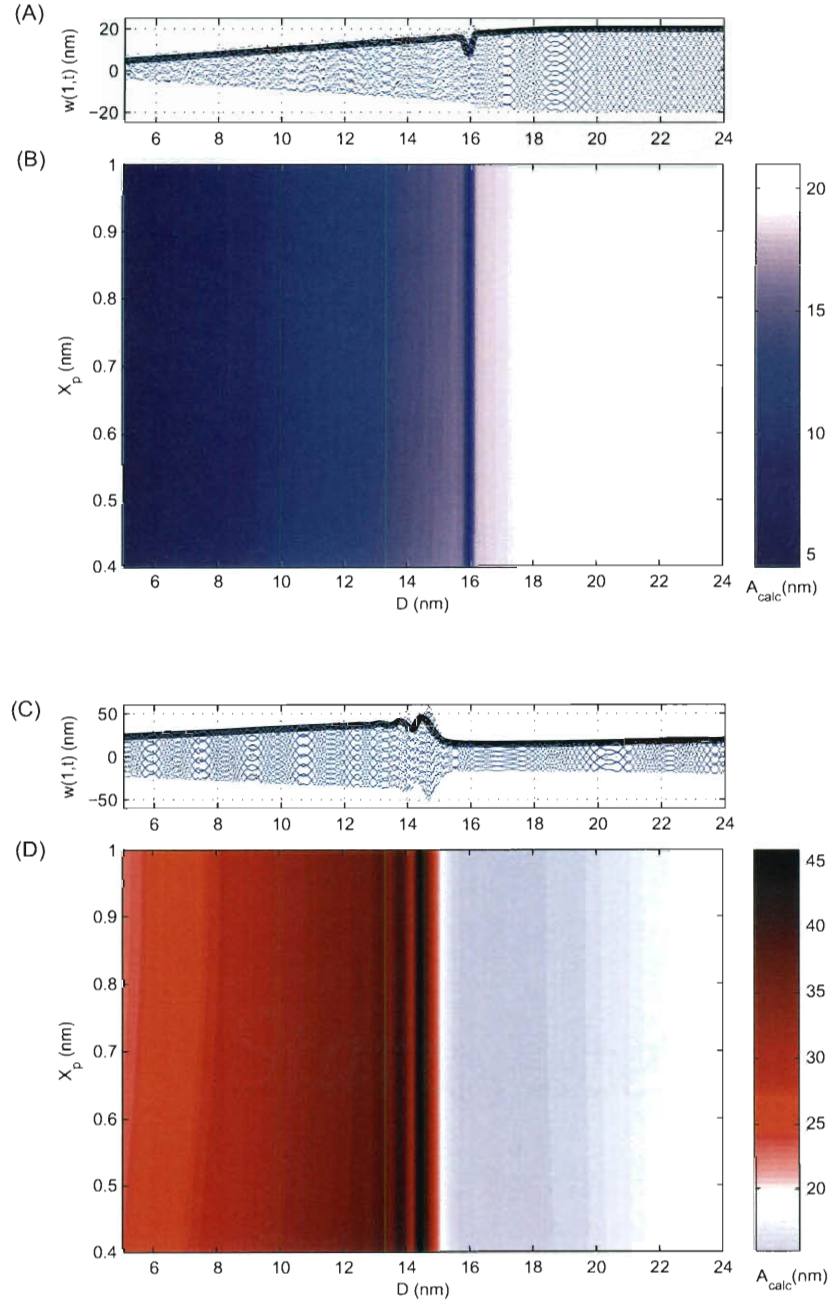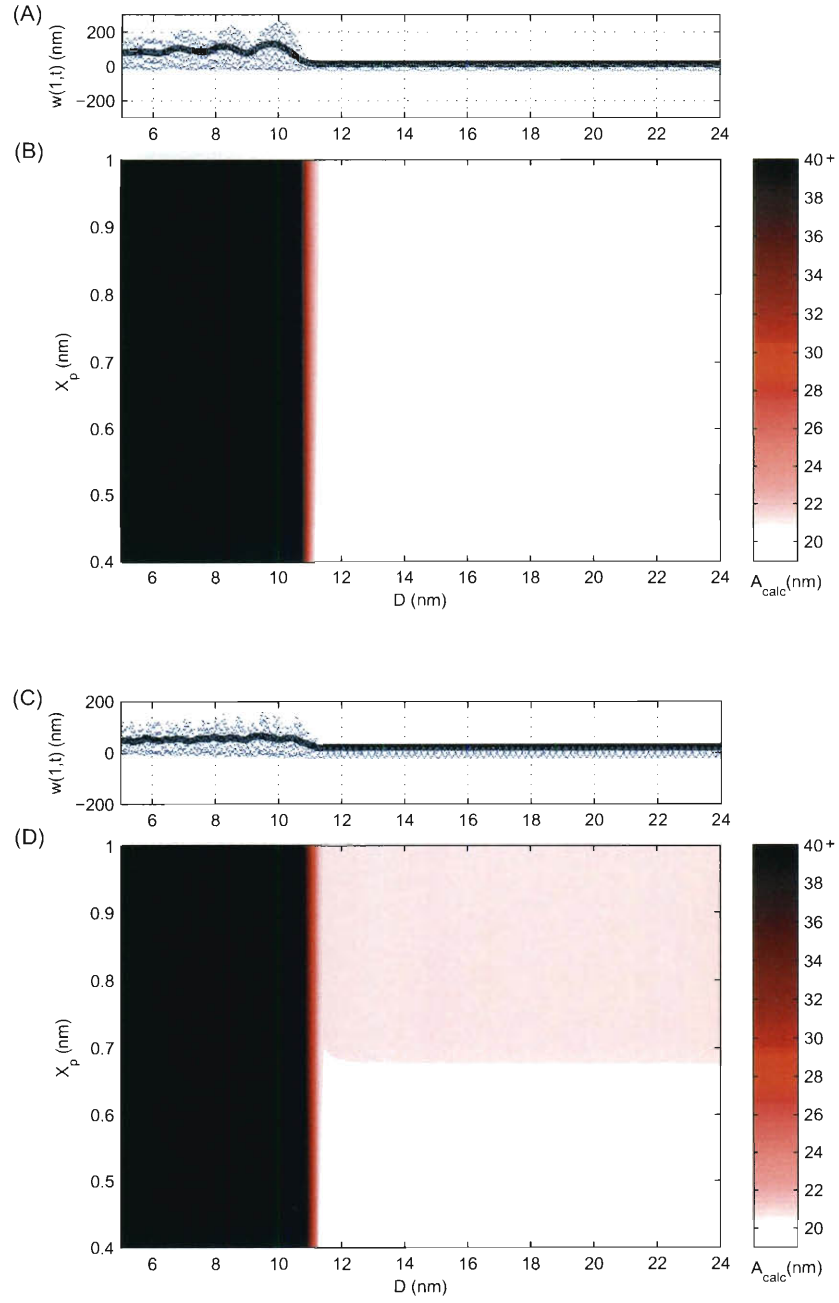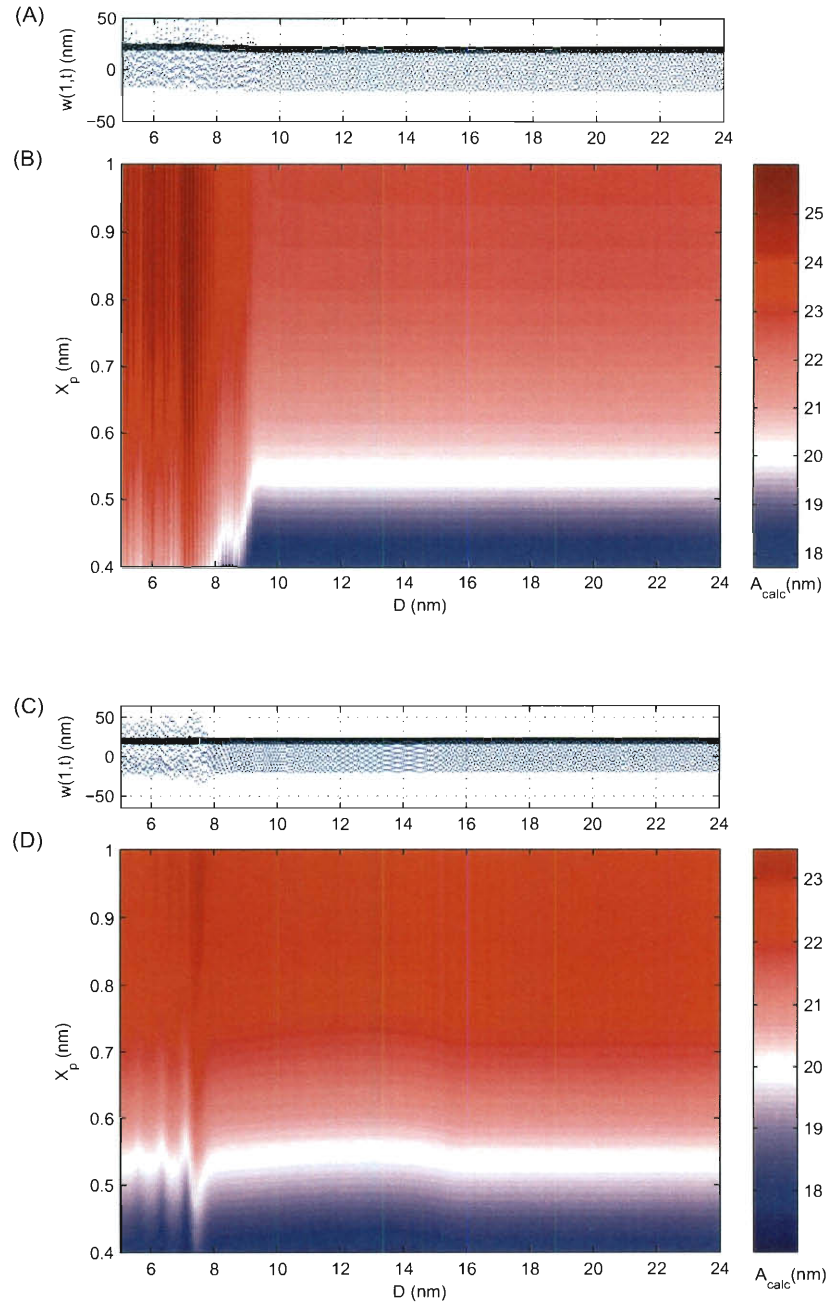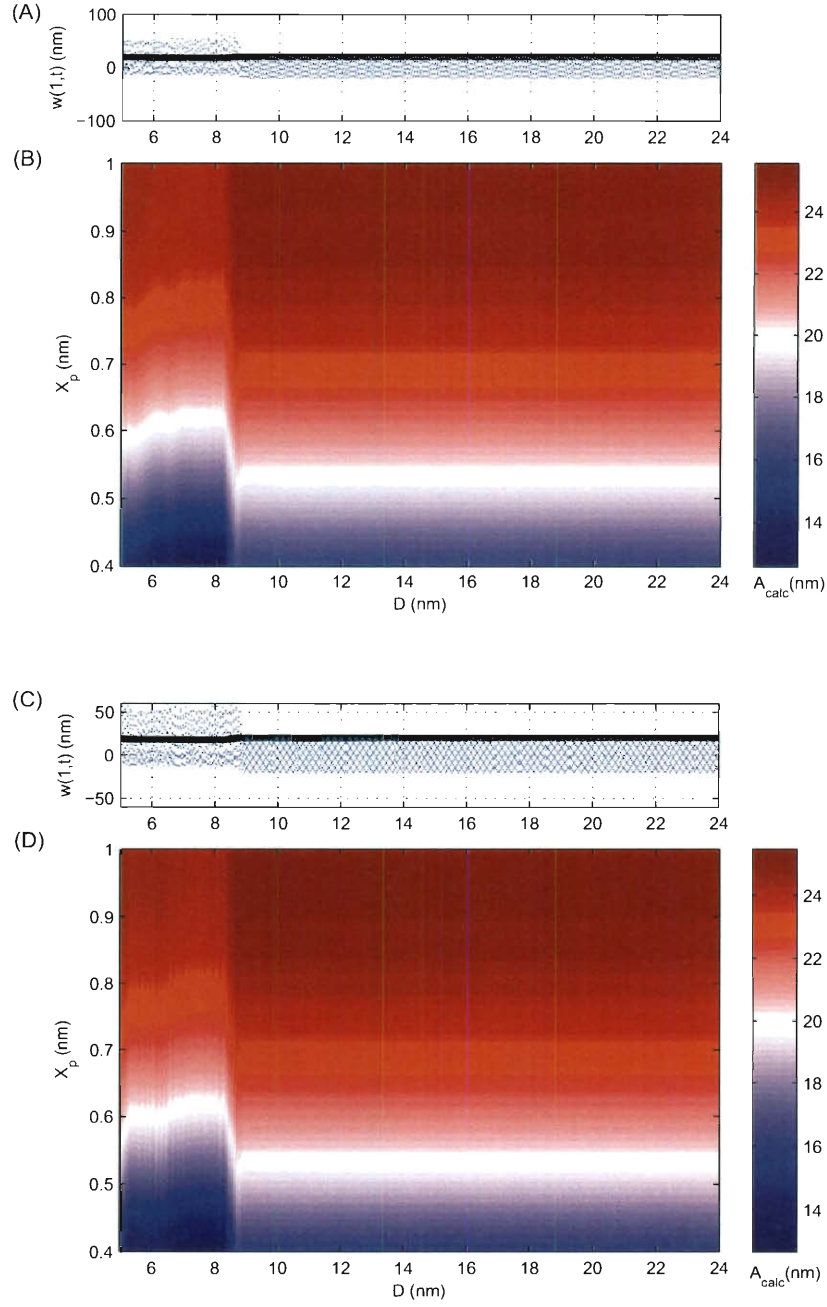
Figure 4.9: (A) Time response (DOTTED) and corresponding amplitude (THICK) and (B) calculated tip amplitude (SHADED) versus spot position and separation distance for $\omega_{ex} = 2.5 \times \omega_1$, $A_{free} = 20$ nm, and $E^* = E^*_{glass}$; (C) and (D) provide similar illustrations for $E^* = 10 \times E^*_{glass}$

profile throughout. Consistent response profile is when the calculated response amplitudes maintain the same distribution for all separation distances over the range of investigation. In this case, the calculated amplitudes are independent of choice of X_p at each separation distance, indicating that the response is dominated by the fundamental mode shape despite significant interactions with the surface that reduce its amplitude by over 60% at $E^* = E^*_{glass}$ and double its amplitude in the increased stiffness case of $E^* = 10 \times E^*_{glass}$. Only a slight deviation from this trend is observed for spot positions near the midpoint and separation distances below 16 nm, resulting in slightly higher calculated amplitude than the corresponding measurements near the tip, around 1 nm.

In Fig. 4.7, actual response amplitude is constant near the free response amplitude of 20 nm in both cases until an abrupt transition into a high amplitude oscillation regime, an expected response for a stiff sample. Measured amplitudes from the response at $D < 11$ nm are on the order of 100 nm. Rather than redefine the color scheme to include these amplitudes, values above 40 nm have been shaded black to maintain easy comparison between each of the figures. A slight spatial dependence in the calculated measurement amplitude is now observed for free response conditions, due to the off-resonance excitation only, maintaining the same profile until the transition into the high amplitude response.

Figures 4.8 and 4.9 demonstrate similar behavior. Measured amplitude varies based on spot position for the free response condition (highest separation distance), its relation relative to the actual amplitude matching the displacement calculation error trend in Fig. 3.6 for $\gamma = 0.03$. The response profile remains consistent, indicated by the parallel horizontal shading, until a sharp transition to a high amplitude response around 8 nm.

To better characterize the response behavior and transitions observed in Figs. 4.6–4.9, a number of supplementary plots are displayed. Two representative cases

from the previous simulations are presented: Fig. 4.10 for excitation at $1.5 \times \omega_1$, and Fig. 4.11 at $2.5 \times \omega_1$, $E^* = E^*_{glass}$. Within each figure, panels (A) and (B) display the frequency spectra of the response before significant influence of the interaction forces and during intermittent contact with the sample surface, respectively. Frequency content is presented using a log scale to observe both large and small components. Panel (C) illustrates the Poincaré section of the response as the separation distance is decreased, and panels (D) and (E) show the phase portrait of the response at the respective separation distances from (A) and (B).

Prior to surface interaction in the first case, $1.5 \times \omega_1$, a strong frequency component corresponding to the excitation frequency is observed from the spectra in Fig. 4.10(A) in addition to a component five orders of magnitude smaller observed at the probe's fundamental frequency—an artifact of transient vibrations. The phase portrait in panel (D) confirms that this initial response is essentially simple harmonic. Upon contact with the surface, a superharmonic component at twice the excitation frequency becomes significant and is accompanied by smaller broadband frequency content. The response transition to the high amplitude regime is clearly observed in both panels (C) and (E), but the irregular response behavior and large jump in response amplitude below $D = 11\ nm$ make it unlikely that these conditions would be utilized in experimental applications. Therefore, for this excitation condition the focus is placed on the response prior to the transition.

As expected, similar qualitative behavior is observed prior to interaction with the surface in Fig. 4.11, $\omega_{ex} = 2.5 \times \omega_1$. In this case, however, the response transition as the separation distance decreases appears more abrupt. Significant contribution from the subharmonic at half the excitation frequency is observed in both the phase portrait and the frequency spectrum, effectively doubling the period of the response. The qualitative behavior of the response transition at $D = 8\ nm$ suggests the presence of a Secondary Hopf bifurcation, which has been observed in previous work under

Figure 4.10: Frequency response spectra for (A) D = 25 − 26 nm and (B) D = 9.8 − 10 nm, (C) Poincaré section of tip response versus separation distance and phase portraits of tip response for (D) 25 − 26 nm and (E) 9.8 − 10 nm; $\omega_{ex} = 1.5 \times \omega_1$, $A_{free} = 20\ nm$, and $E^* = E^*_{glass}$.

these conditions. If the separation distance was decreased in incremental steps and the transient behavior allowed to completely decay, a much sharper transition would be expected in the Poincaré section. This bifurcation could have potential utility in future experimental work in a similar manner as the period doubling bifurcation in Ref. [11], for example. The results presented within this thesis would therefore be useful to estimate the measurement accuracy during operation at these conditions. A method for estimating the measurement accuracy using standard or—in this case— novel feedback control is presented in Section 4.3.3.
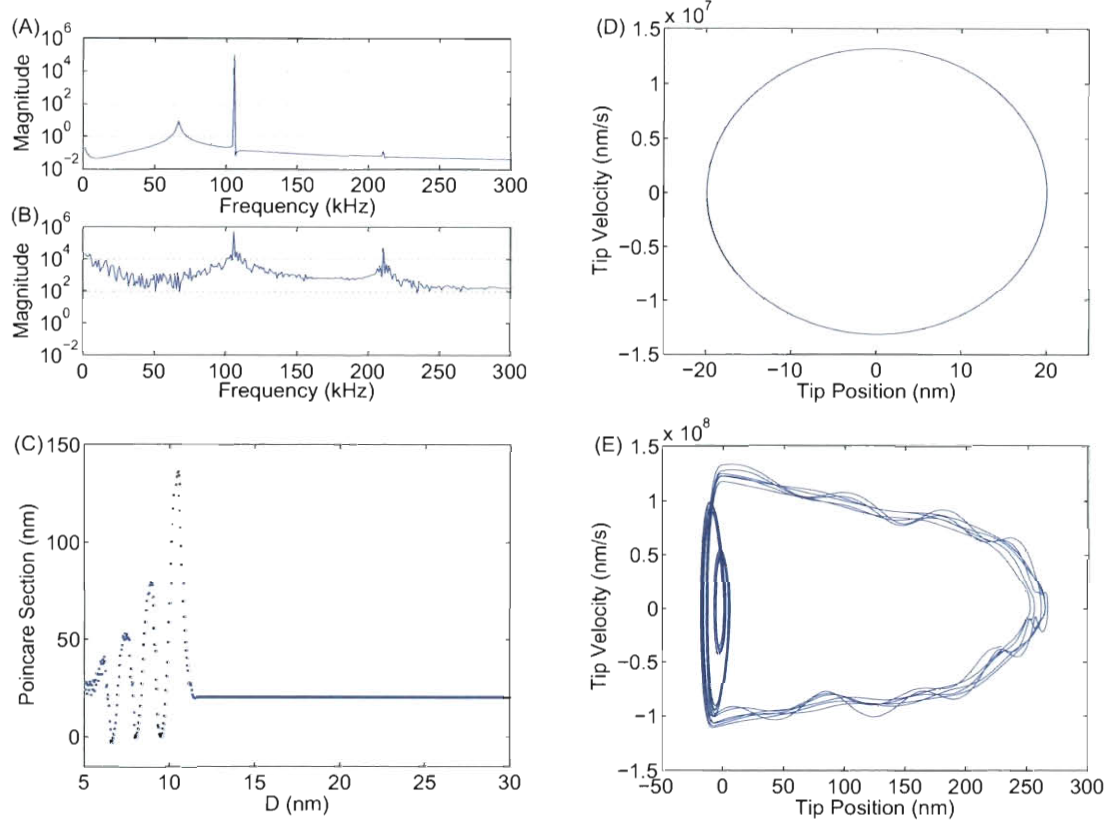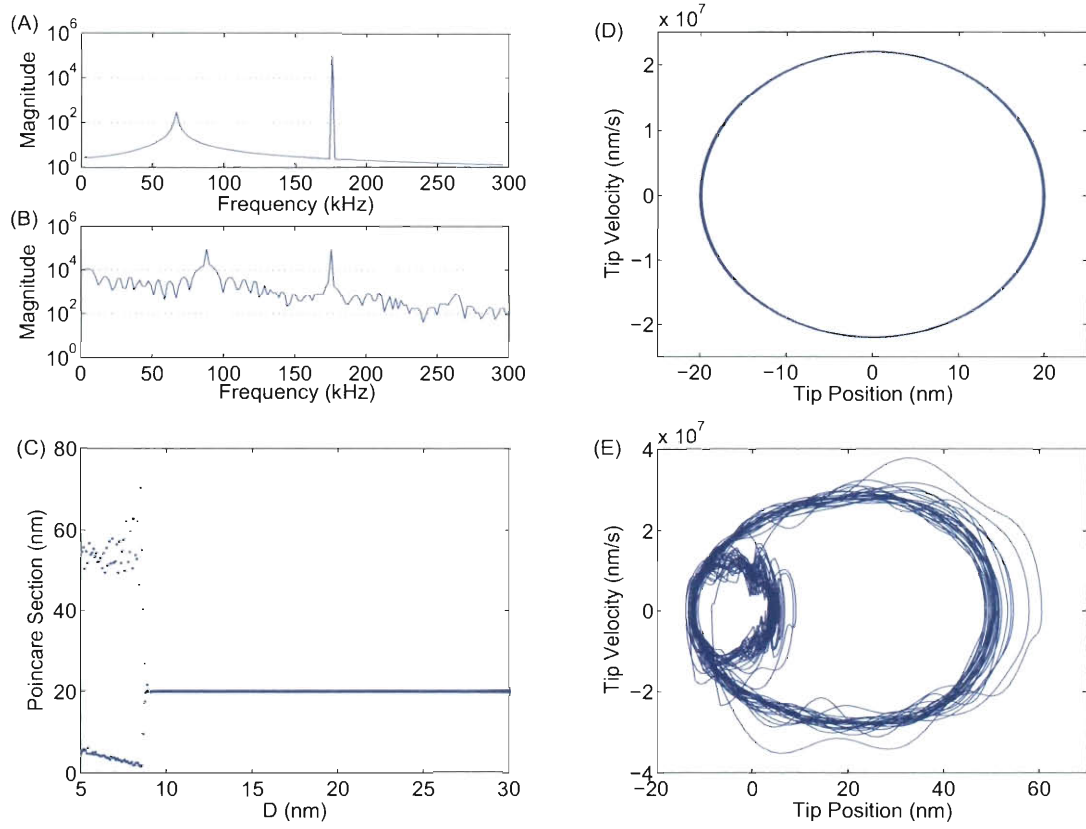
Figure 4.11: Frequency response spectra for (A) $D = 25 - 26$ nm and (B) $D = 5 - 7.5$ nm, (C) Poincaré section of tip response versus separation distance and phase portraits of tip response for (D) $25 - 26$ nm and (E) $5 - 7.5$ nm; $\omega_{ex} = 2.5 \times \omega_1$, $A_{free} = 20$ nm, and $E^* = E^*_{glass}$.

4.3.2 Response Amplitude Versus Separation Distance on Silicone Rubber Sample

Figures 4.12–4.15 illustrate the same simulations performed on the rubber sample. Again, free response amplitude is tuned to 20 nm. An initial separation distance of 58 nm is chosen such that the probe is initially no closer than 10 nm to the force threshold at $D = 27.6$ nm in the cases where $E^* = E^*_{rubber}$. For the first case at the fundamental frequency, Fig. 4.12 (A) and (B), the response amplitude decreases as the probe enters the attractive regime, then increases as it continues into the repulsive regime. Calculated response is again independent of spot position, indicating a consistently strong first mode response component for all separation distances. Panels (C) and (D) exhibit similar behavior, though scaled into a smaller range of separation distance values, reflecting the manner in which the interaction force profile changes with effective modulus (Fig. 4.1).

Figures 4.13–4.15, corresponding to off-resonance excitation cases $\omega_{ex} = 1.5\times$, $2.0\times$, and $2.5 \times \omega_1$, exhibit the same trend that the response profile is not significantly affected by the interaction forces. The behavior most prominently observed between $D = 17$ and 37 nm in Fig. 4.13 is due to the true response amplitude increase when significant contribution from the interaction forces are experienced. The influence of the surface forces on the probe response is severely diminished for both effective modulus values at $\omega_{ex} = 2.0\times$ and $2.5 \times \omega_1$ due to the higher kinetic energy of the probe during the interactions.

Similar to the response quantities plotted in Figs. 4.10 and 4.11 for the glass sample, Fig. 4.16 illustrates the changes to the response behavior for intermittent contact with the rubber sample at $2.5 \times \omega_1$, $E^* = E^*_{rubber}$. Again, a strong spectral component is observed at the excitation frequency and a small component observed at the probe's fundamental frequency for response away from the surface interaction. Upon interaction with the sample surface, the response appears to remain essen-

Figure 4.12: (A) Time response (DOTTED) and corresponding amplitude (THICK) and (B) calculated tip amplitude (SHADED) versus spot position and separation distance for $\omega_{ex} = \omega_1$, $A_{free} = 20 \ nm$, and $E^* = E^*_{rubber}$; (C) and (D) provide similar illustrations for $E^* = 10 \times E^*_{rubber}$.

Figure 4.13: (A) Time response (DOTTED) and corresponding amplitude (THICK) and (B) calculated tip amplitude (SHADED) versus spot position and separation distance for $\omega_{ex} = 1.5 \times \omega_1$, $A_{free} = 20$ nm, and $E^* = E^*_{rubber}$; (C) and (D) provide similar illustrations for $E^* = 10 \times E^*_{rubber}$.
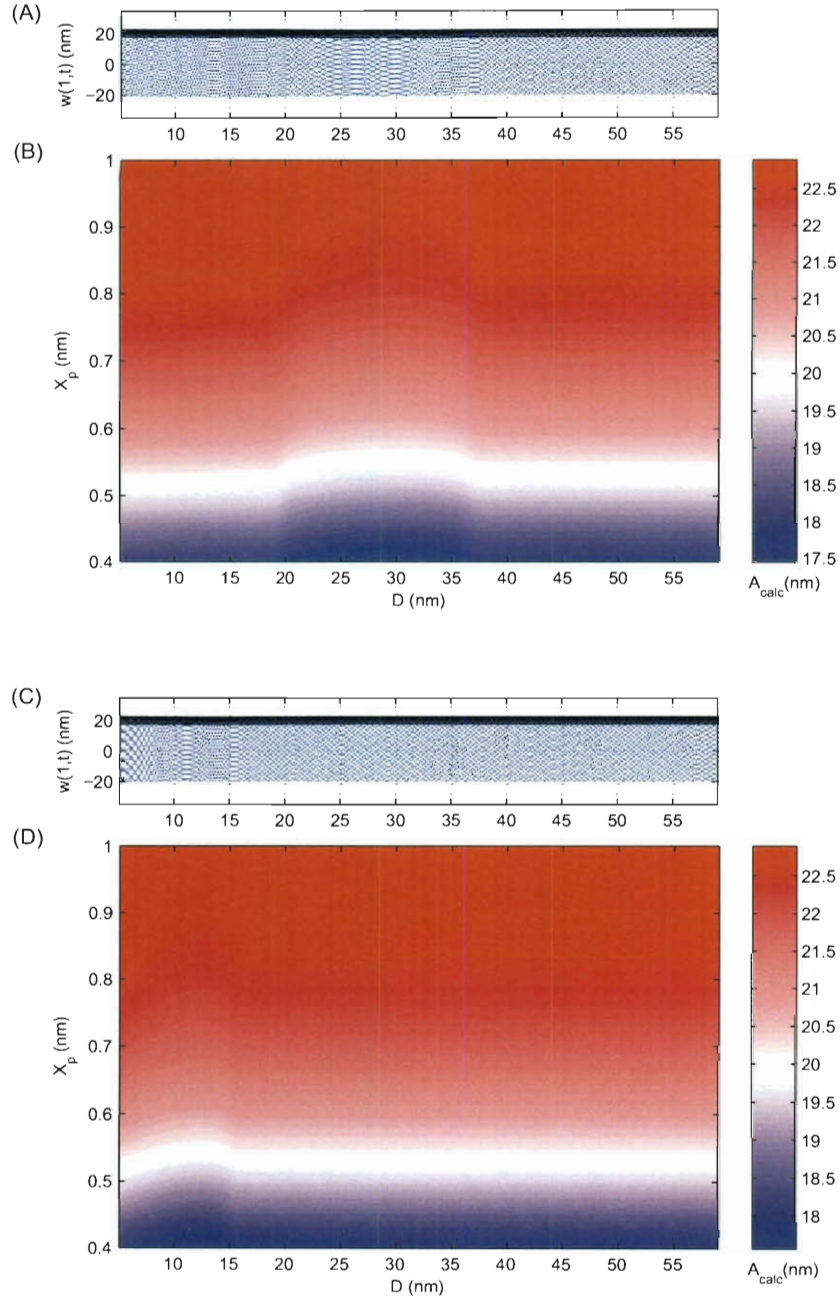
Figure 4.14: (A) Time response (DOTTED) and corresponding amplitude (THICK) and (B) calculated tip amplitude (SHADED) versus spot position and separation distance for $\omega_{ex} = 2 \times \omega_1$, $A_{free} = 20\ nm$, and $E^* = E^*_{rubber}$; (C) and (D) provide similar illustrations for $E^* = 10 \times E^*_{rubber}$.
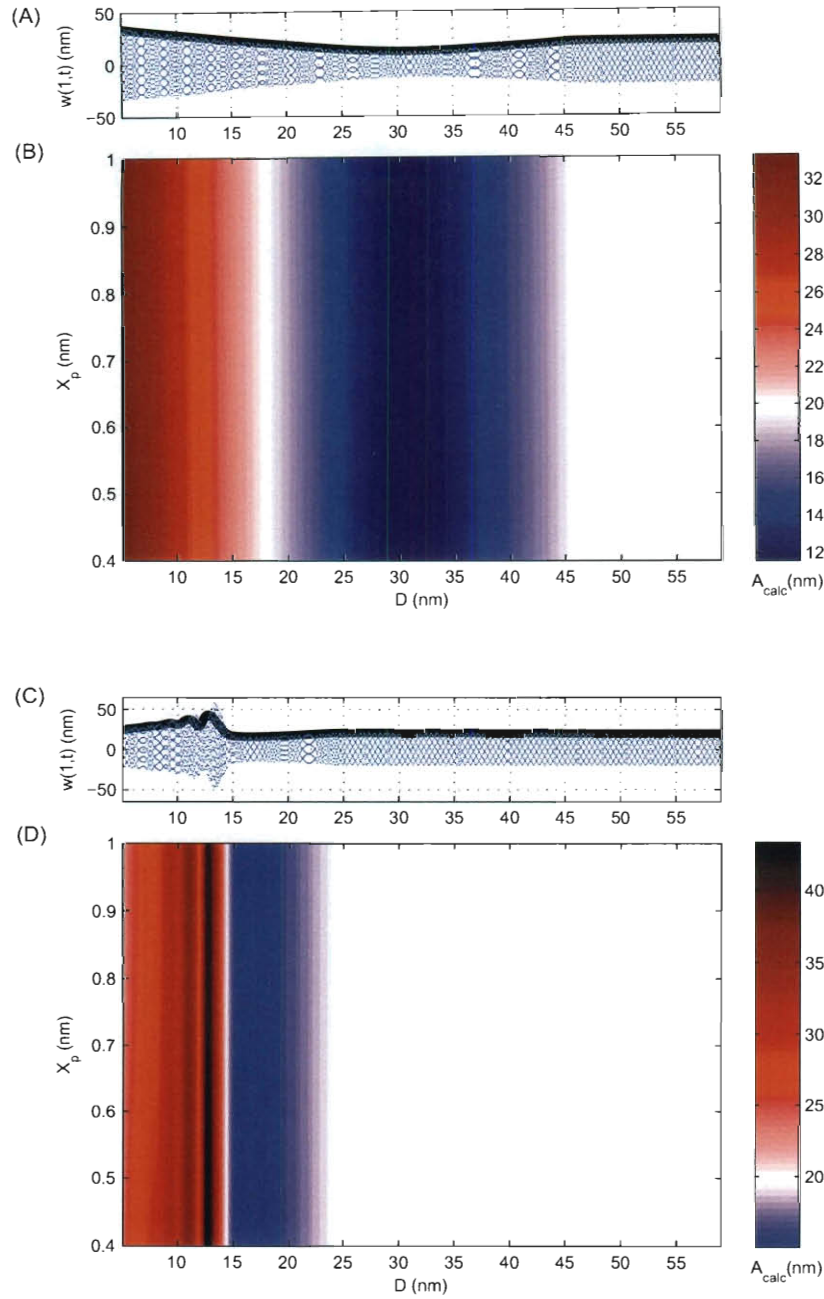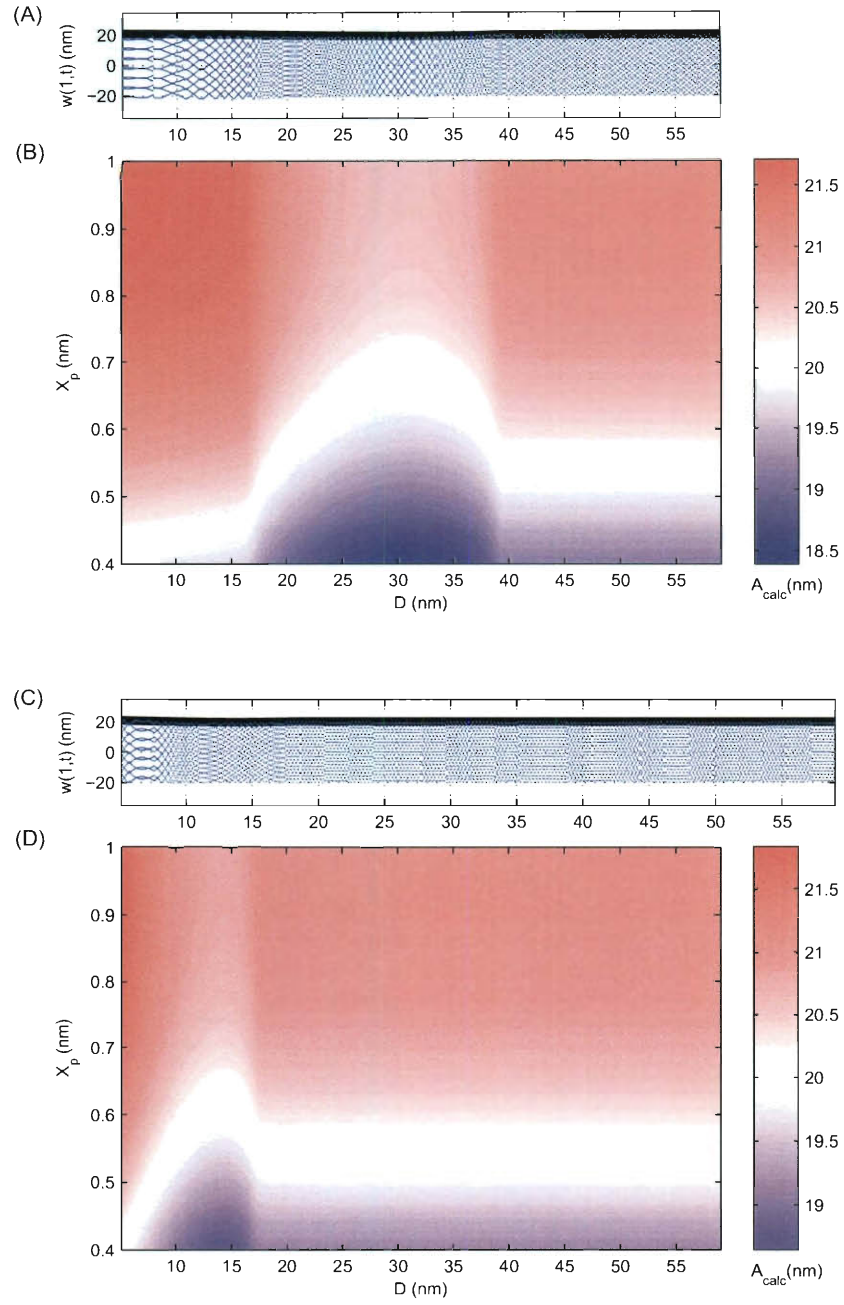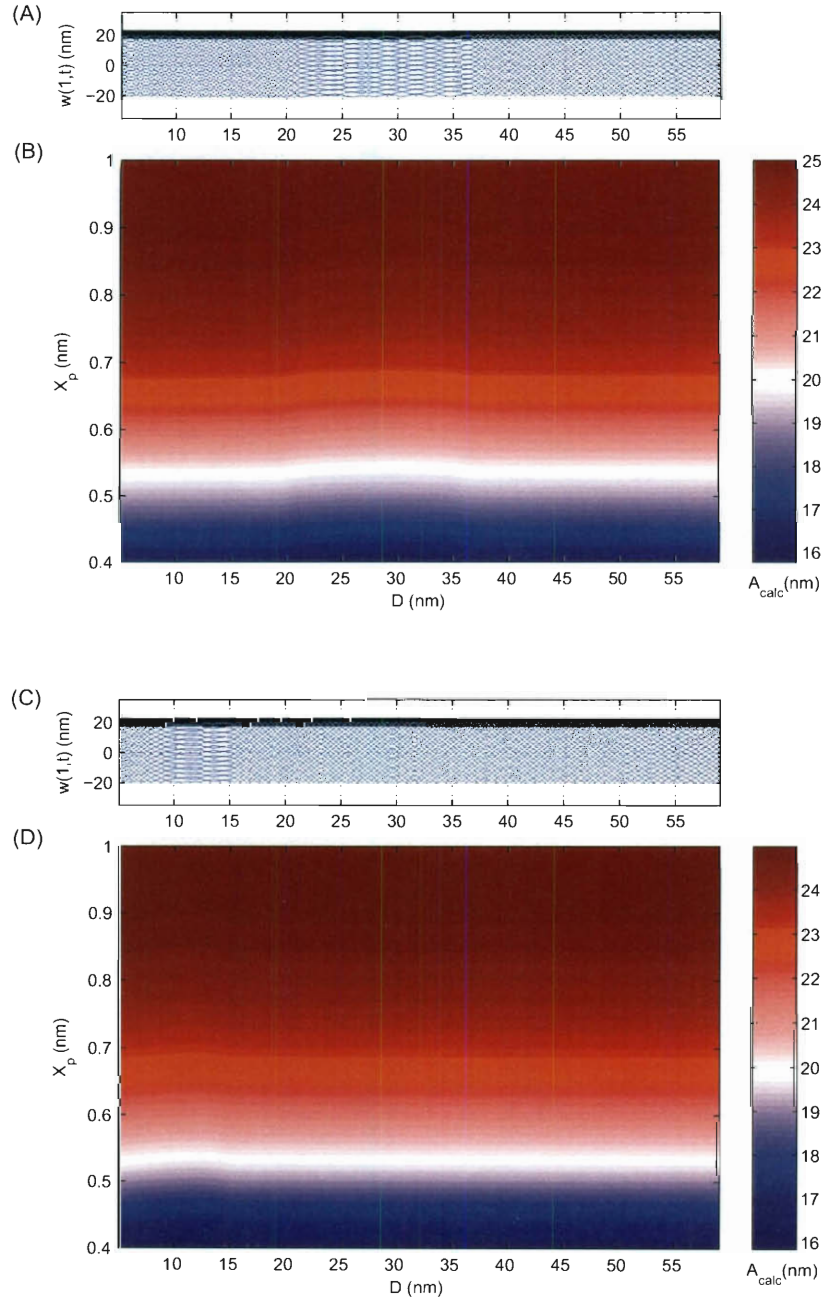
Figure 4.15: (A) Time response (DOTTED) and corresponding amplitude (THICK) and (B) calculated tip amplitude (SHADED) versus spot position and separation distance for $\omega_{ex} = 2.5 \times \omega_1$, $A_{free} = 20 \ nm$, and $E^* = E^*_{rubber}$; (C) and (D) provide similar illustrations for $E^* = 10 \times E^*_{rubber}$.
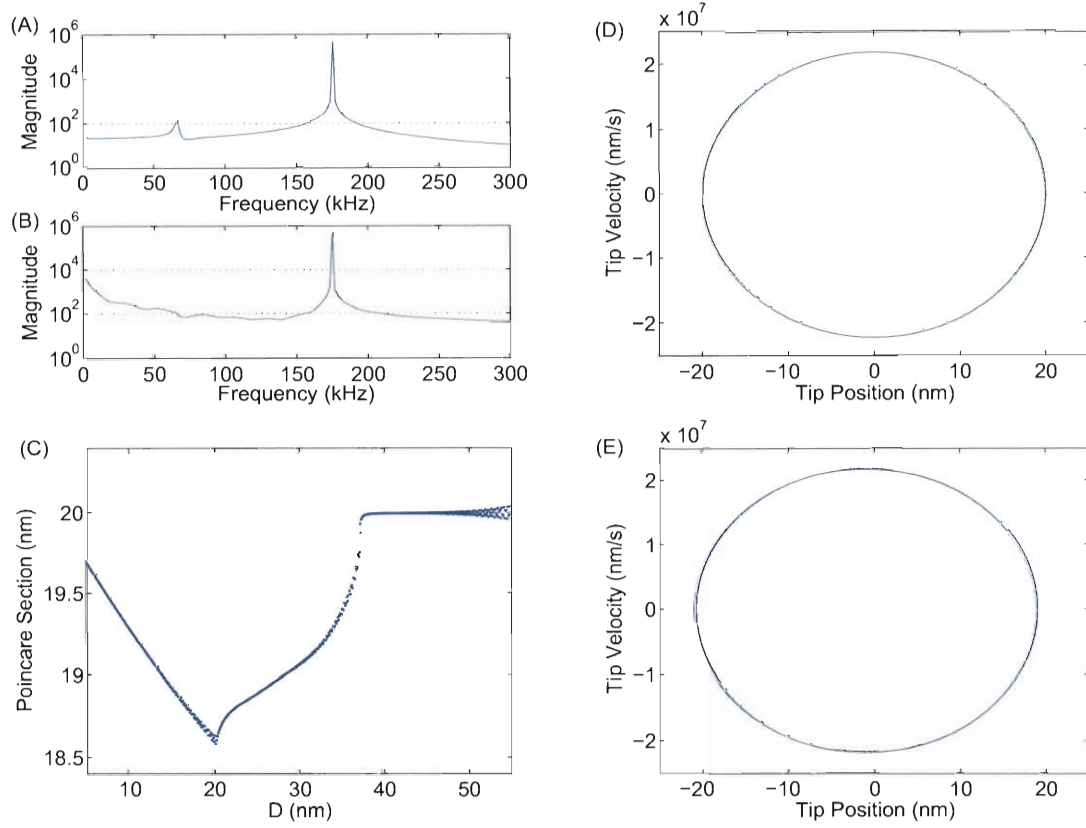
Figure 4.16: Frequency response spectra for (A) D = 55 − 57 nm and (B) D = 26 − 28 nm, (C) Poincaré section of tip response versus separation distance and phase portraits of tip response for (D) 55 − 57 nm and (E) 26 − 28 nm; $\omega_{ex} = 2.5 \times \omega_1$, $A_{free} = 20$ nm, and $E^* = E^*_{rubber}$.

tially simple harmonic, with the only significant frequency component matching the excitation. The Poincaré section displays a small but smooth dip in the response amplitude centered around $D = 20\ nm$. Examining each of the panels, it is clear that the period doubling bifurcation has not been encountered for these conditions, likely requiring larger compression of the sample. However, these results are important to characterize the measurement accuracy under similar conditions immediately prior to bifurcation.

4.3.3 Estimation of Vertical Measurement Error from Response Amplitude Plots

By comparing panels (B) and (D) in each figure, it is possible to estimate the vertical measurement error for certain applications. The data is presented in this manner to give the most useful information to conduct measurement accuracy estimations given a particular application. As an example, Fig. 4.17 illustrates this process as applied to Fig. 4.12 to estimate the vertical measurement accuracy for the same conditions as the PID control implementation in Section 4.2.3.

Recall that the controller operates by adjusting the separation distance until the set point amplitude is achieved. So, to estimate vertical measurement accuracy during this $10\times$ effective modulus increase for a set point of 90%, first the separation distance is located on the left panel of Fig. 4.17 where the 18 nm response amplitude is observed at a spot position of, say, $X_p = 0.9$. In this case, the calculated amplitude is independent of spot position; so $D = 42\ nm$ for all X_p. Note that an 18 nm response amplitude is also observed at $D = 22\ nm$ (marked with an $\times$), but in practice the probe would initially approach from a higher separation distance and first reach its set point at $D = 42\ nm$.

Next, calculate the location that the probe will have moved to after the effective modulus change, i.e. locate D in the right panel of Fig. 4.17 corresponding to
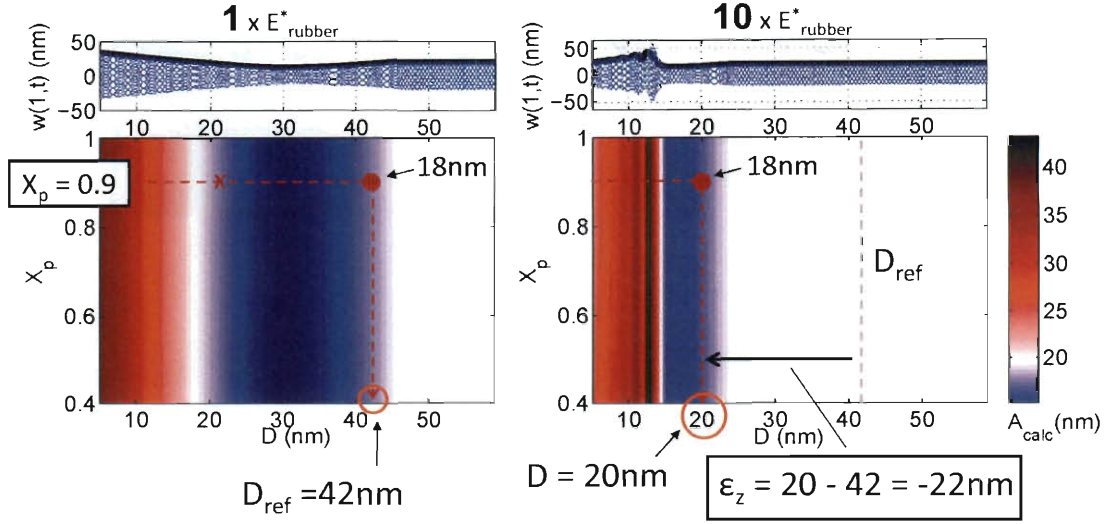
Figure 4.17: Estimation of vertical measurement error using amplitude contour plots.

$X_p = 0.9$, $A = 18$ nm; in this case $D = 20$ nm. The estimated vertical measurement error due to the effective modulus change is therefore the amount the controller has moved, or 22 nm, an estimation which agrees with the results from the actual controlled simulation illustrated in Fig. 4.5.

It is concluded from Figs. 4.6–4.15 that, although the nonlinear surface forces certainly influence both the response amplitude and characteristics, the excitation frequency has a much higher influence on the response profile than the nonlinear tip sample interaction forces. Effective modulus increases of up to 10 times have been demonstrated to affect the true response amplitude and in the case of the silicone rubber, significantly decrease the range of interaction according to the movement of the force threshold (see Fig. 4.5), but the response generally maintains the profile determined by the excitation frequency. Therefore the only significant vertical measurement error corresponds to the movement of the force threshold. This is considered a result of the chosen form of Eqn. (2.43), where the surface boundary is defined as the location between the attractive and repulsive regimes where zero force is experienced. Utilizing a coordinate system where the surface is defined by the outer

boundary of the attractive regime would eliminate this error.

4.3.4 Displacement Measurement Error for Intermittent Contact Operation

As a final example to complete the scope of the measurement accuracy study for off-resonance excitation in tapping-mode AFM, the results from Figs. 4.6 and 4.13 are presented in another manner which may provide useful in to alternate applications and general research at off-resonance conditions. The contour plots in Figs. 4.18 and 4.19 illustrate the percent difference between calculated and actual tip response amplitude versus spot position and separation distance, with top and bottom contour plots again representing $E^* = E^*_{rubber}$ and $10 \times E^*_{rubber}$. Actual response amplitude corresponding to each case is included for reference in panels (A) and (C).

Whereas the presentation of Figs. 4.6 and 4.15 are tailored to more easily compare measurement accuracy for scanning modes, Figs. 4.18 and 4.19 provide an evaluation of how accurately the calculated response amplitude matches the true response amplitude, using the same calculation method as in Chapter 3. Again, this measurement is not directly correlated to accuracy in common scanning modes, but is rather considered most useful for research applications at off-resonance excitation where an accurate knowledge of tip displacement is of primary importance.

By examining Fig. 4.18 (B) and (D), it is observed that spot positions located near the tip exhibit a $5 - 6\%$ overestimation of the response amplitude during the range of separation where the amplitude is changing with D. However, the spot position just above $X_p = 0.5$ maintains accurate response amplitude calculations within 0.5% of the actual value throughout the range of separation distances.

Figure 4.19 provides an even more drastic example. In both panels (B) and (D) a laser spot positioned between $X_p = 0.5$ and 0.6 is still able to accurately calculate the response amplitude after the response abruptly transitions to the high

amplitude regime. In fact, the same behavior is observed when plotting each of the responses from 4.6–4.15 in this manner. As illustrated in Fig. 3.3, a spot position near $X_p = 0.52$ exhibits the same relationship between slope and displacement at this off-resonance frequency as at the fundamental response frequency, corresponding to calibration conditions. The robustness of the spot position between $X_p = 0.5$ and 0.6 to maintain accurate displacement prediction has been demonstrated in this work using both hard and soft samples.

Figure 4.18: (A) True response amplitude and (B) displacement measurement error ε (SHADED) versus spot position and separation distance for $\omega_{ex} = 1.5 \times \omega_1$, $A_{free} = 20\ nm$, and $E^* = E^*_{rubber}$; (C) and (D) provide similar illustrations for $E^* = 10 \times E^*_{rubber}$.
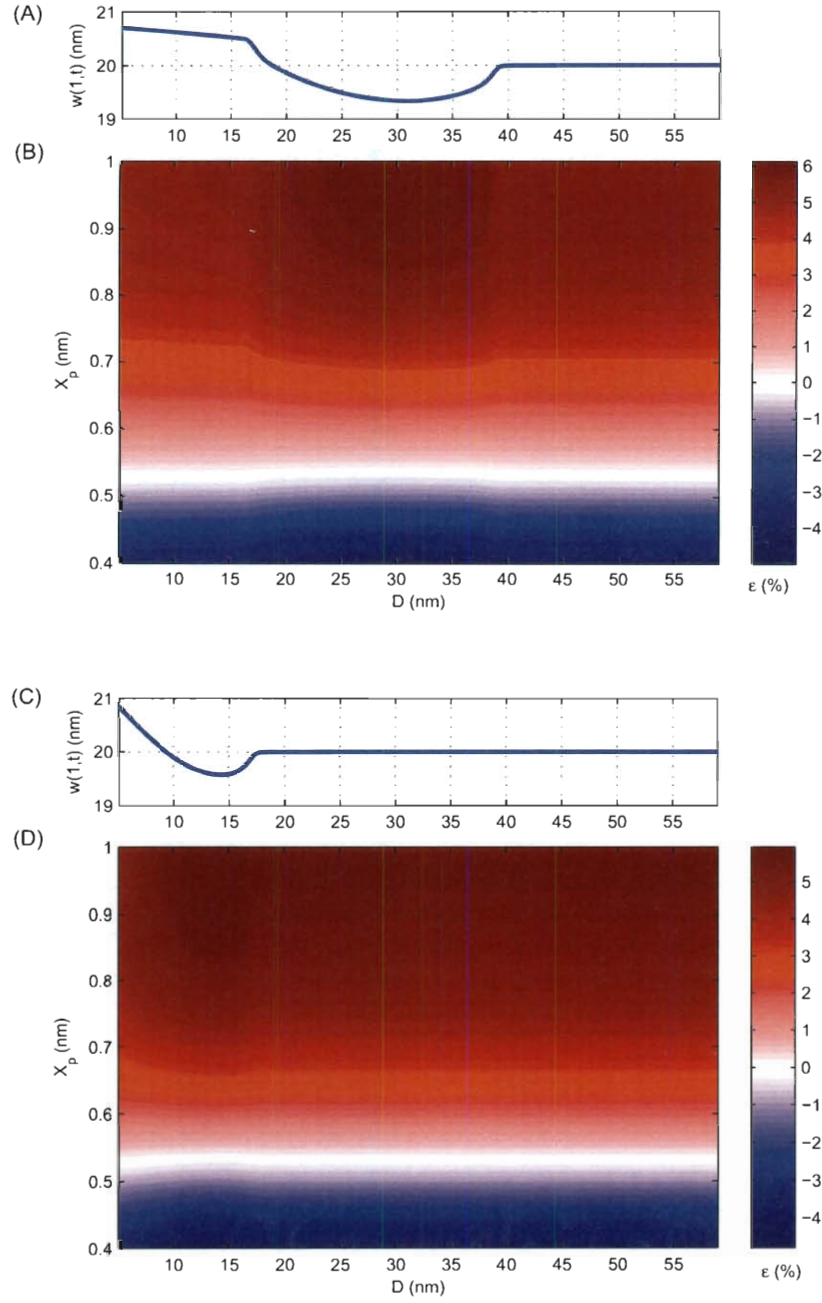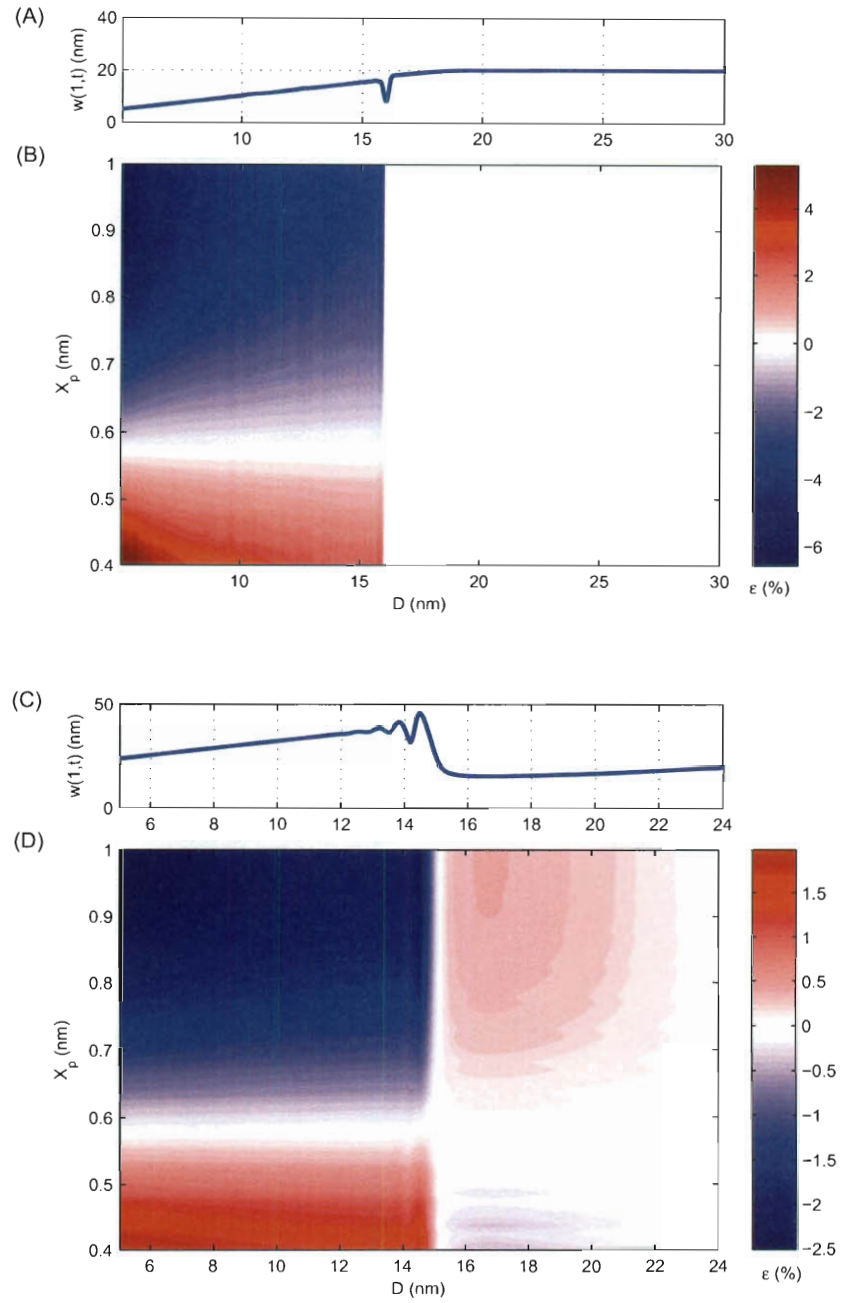
Figure 4.19: (A) True response amplitude and (B) displacement measurement error ε (SHADED) versus spot position and separation distance for $\omega_{ex} = \omega_1$, $A_{free} = 20\ nm$, and $E^* = E^*_{glass}$; (C) and (D) provide similar illustrations for $E^* = 10 \times E^*_{glass}$.

Chapter 5

Conclusions

5.1 Concluding Remarks

Optical lever measurement accuracy was studied for a dynamic AFM system for resonant and off-resonance excitation for a range of different system parameter values. The most pronounced contribution of this work is the identification of a spot position range $X_p = 0.5$ to 0.6 within which the measurement error is zero under free response conditions and minimal during intermittent contact. Measurement error was determined to decrease for smaller values of tip mass for off-resonance conditions. Less than 1 nm error was observed for simulated AM-AFM scans at the fundamental frequency as the effective modulus was increased to 10 times its original value, confirming the accuracy of the optical lever method in this application.

Equations of motion were derived from the Euler-Bernoulli beam equation with additional terms accounting for tip mass, base excitation and nonlinear surface forces. A numerical model was developed from the equations of motion to study the response of the probe for different values of the excitation frequency, spot position, tip mass, quality factor, separation distance and surface force parameters.

Measurement accuracy was quantified in two ways. In the first method, displace-

ment measurement error ε was defined to represent the percent difference between the tip displacement calculated from the photodetector voltage signal and calibration equation and the actual tip displacement directly observed from the probe's response. This error measure provides a more general evaluation of how well the optical lever measurement captures the response, and is most applicable in research applications where accurate knowledge of the response amplitude is important.

The second error metric ε_Z provides an application-specific measurement of the vertical error during AM-AFM scanning, a direct cause of image distortion. In order to calculate this measurement, feedback control was implemented within the numerical model to simulate actual AM-AFM operation. Scans of an atomically flat surface with linearly increasing effective modulus were simulated and the z-movement of the base from the reference distance was identified as the error ε_Z.

Simulations were conducted for free response conditions and intermittent contact with a sample surface. Displacement measurement error was determined to be independent of quality factor for $Q > 10$. This suggests that the results from the numerical model were not only specific to the particular quality factor used. Zero measurement error was confirmed at the fundamental frequency regardless of tip mass and spot position, verifying the value of the optical lever method in traditional AFM applications.

Larger tip mass values were determined to produce greater displacement measurement error for off-resonance conditions. Added tip mass from surface contaminants or matter intentionally bonded to the probe decrease the measurement accuracy at these higher frequencies. Researchers should consider lower tip mass probes for off-resonance applications when possible to produce the most accurate measurements.

The robustness of the optical lever system to variations in effective modulus of the sample surface during AM-AFM operation was verified for operation at the fundamental frequency. Vertical measurement error ε_Z was determined for scans on a

soft silicone rubber material and a hard glass sample. In each case, effective modulus was increased linearly during the scan to ten times its original value. Subnanometer vertical measurement error was observed for all scans on the glass sample. Vertical measurement error for the rubber material directly correlated to the movement of the attractive interaction force threshold, and therefore the system can be considered to have accurately tracked the movement of the effective surface. In both cases, the results show that the higher mode contributions from the increased interaction forces from higher effective modulus values did not produce significant response profile changes. It can be concluded that the optical lever method can be used with confidence to provide high accuracy measurements in AM-AFM at the fundamental frequency.

Spot location was determined to have a significant effect on measurement accuracy due to profile changes from the additional influence of higher mode shapes during off-resonance excitation. For each mass ratio, a spot position between $X_p = 0.5$ and 0.6 was identified which produced zero measurement error during off-resonance excitation and free response conditions. This specific point corresponds to the location where the slope-displacement relationship from the first mode is preserved after modal contributions from the second mode. Intermittent contact simulations with a soft silicone rubber material and a hard glass sample confirmed that the highest measurement accuracy, near zero in most cases, was achieved at a spot position between $X_p = 0.5$ and 0.6. The laser spot should be positioned within this range during off-resonance operation to most accurately measure probe displacement.

5.2   Future Work

Based on the results of this study, potential areas for future work include experimental verification, submerged operation and hysteretic interactions. Experimental work

would be helpful to confirm higher measurement accuracy at spot positions near the midpoint, though the challenge of capturing the actual response for comparison arises. It may be possible to construct an experimental setup using a multi-laser system to simultaneously measure and compare the response signal at multiple spot positions. Refinement of the numerical model to account for submerged operation in a liquid environment would be useful to expand the scope of this work to additional AFM applications, and the use of an alternate force model, such as the JKR interaction model, would allow the scope of the work to be extended to materials with a significant attractive regime, or those whose properties result in force hysteresis between the probe's approach and retraction.

Bibliography

[1] G. Binnig, C. Quate, and C. Gerber, "Atomic force microscope", *Physical review letters*, **56** (1986) 930–933.

[2] J. Humpolíčková, A. Benda, R. MacHáň, J. Enderlein, and M. Hof, "Dynamic saturation optical microscopy: Employing dark-state formation kinetics for resolution enhancement", *Physical Chemistry Chemical Physics*, **12** (2010) 12457–12465.

[3] J. Yang, "MEMS-based probe recording technology", *Journal of Nanoscience and Nanotechnology*, **7** (2007) 181–192.

[4] F. Giessibl, "Advances in atomic force microscopy", *Reviews of modern physics*, **75** (2003) 949–983.

[5] T.R. Albrecht, P. Grütter, D. Horne, and D. Rugar, "Frequency modulation detection using high-Q cantilevers for enhanced force microscope sensitivity", *Journal of Applied Physics*, **69** (1991) 668–673.

[6] M. Lee and W. Jhe, "General theory of amplitude-modulation atomic force microscopy", *Physical Review Letters*, **97** (2006) 1–4.

[7] P. Eaton and P. West, *Atomic force microscopy*. Oxford University Press, 2010.

[8] W. Chin, E. Ott, H.E. Nusse, and G. Celso, "Grazing bifurcations in impact oscillators", *Physical Review E*, **50** (1994) 4427–4444.

[9] P. Thota and H. Dankowicz, "Continuous and discontinuous grazing bifurcations in impacting oscillators", *Physica D*, **214** (2006) 187–197.

[10] A. Dick, B. Balachandran, H. Yabuno, M. Numatsu, K. Hayashi, M. Kuroda, and K. Ashida, "Utilizing nonlinear phenomena to locate grazing in the constrained motion of a cantilever beam", *Nonlinear Dynamics*, **57** (2009) 335–349.

[11] A.J. Dick and W. Huang, "Period-doubling bifurcations in atomic force microscopy", in *ASME International Design Engineering Technical Conference (IDETC)*, (2009).

[12] A.J. Dick and S.D. Solares, "Utilizing off-resonance and dual-frequency excitation to distinguish attractive and repulsive surface forces in atomic force microscopy", *Journal of Computational and Nonlinear Dynamics*, **6** (2011) 1–12.

[13] T.R. Rodríguez and R. García, "Compositional mapping of surfaces in atomic force microscopy by excitation of the second normal mode of the cantilever", *Applied Physics Letters*, **84** (2004) 449–451.

[14] P. Thota, S. MacLaren, and H. Dankowicz, "Controlling bistability in tapping-mode atomic force microscopy using dual-frequency excitation", *Applied Physics Letters*, **91** (2007) 1–3.

[15] O. Pfeiffer, C. Loppacher, C. Wattinger, M. Bammerlin, U. Gysin, M. Guggisberg, S. Rast, R. Bennewitz, E. Meyer, and H. Güntherodt, "Using higher flexural modes in non-contact force microscopy", *Applied Surface Science*, **157** (2000) 337–342.

[16] P.M. Hoffmann, "Dynamics of small amplitude, off-resonance AFM", *Applied Surface Science*, **210** (2003) 140–145.

[17] R. Stark, "Spectroscopy of higher harmonics in dynamic atomic force microscopy", *Nanotechnology*, **15** (2004) 347–351.

[18] H.N. Arafat, A.H. Nayfeh, and E.M. Abdel-Rahman, "Modal interactions in contact-mode atomic force microscopes", *Nonlinear Dynamics*, **54** (2008) 151–166.

[19] T.E. Schäffer and P.K. Hansma, "Characterization and optimization of the detection sensitivity of an atomic force microscope for small cantilevers", *Journal of Applied Physics*, **84** (1998) 4661–4666.

[20] R. Stark, "Optical lever detection in higher eigenmode dynamic atomic force microscopy", *Review of Scientific Instruments*, **75** (2004) 5053–5055.

[21] T. Schäffer and H. Fuchs, "Optimized detection of normal vibration modes of atomic force microscope cantilevers with the optical beam deflection method", *Journal of Applied Physics*, **97** (2005) 1–8.

[22] L.Y. Beaulieu, M. Godin, O. Laroche, V. Tabard-Cossa, and P. Grütter, "A complete analysis of the laser beam deflection systems used in cantilever-based systems", *Ultramicroscopy*, **107** (2007) 422–430.

[23] H. Xie, J. Vitard, S. Haliyo, and S. Régnier, "Calibration and nonlinearity compensation for force application in AFM based nanomanipulation", in *IEEE/RSJ International Conference on Intelligent Robots and Systems*. IEEE, (2008) 4024–4029.

[24] C.-K. Yang, A. Bossche, P.J. French, H. Sadeghian, J.F.L. Goosen, F. van Keulen, K.B. Gavan, H.S.J. van der Zant, and E.W.J.M. van der Drift, "Effect of laser deflection on resonant cantilever sensors", in *IEEE Sensors 2009 Conference*, (2009).

[25] A. Raman, J. Melcher, and R. Tung, "Cantilever dynamics in atomic force microscopy", *Nanotoday*, **3** (2008) 20–27.

[26] R. García and A. San Paulo, "Dynamics of a vibrating tip near or in intermittent contact with a surface", *Physical Review B*, **61** (2000) 381–384.

[27] S.G. Kelly, *Advanced vibration analysis*. CRC Press, 2007.

[28] J. Cleveland and R. Proksch. "Asylum research AFM cantilevers". http://www.asylumresearch.com, 2010.

[29] B. Cappella and G. Dietler, "Force-distance curves by atomic force microscopy", *Surface Science Reports*, **34** (1999) 1–104.

[30] K.L. Johnson, K. Kendall, and A.D. Roberts, "Surface energy and the contact of elastic solids", *Proceedings of the Royal Society of London A*, **324** (1971) 301–313.

[31] D. Maugis, "Adhesion of spheres: the JKR-DMT transition using a Dugdale model", *Journal of Colloid and Interface Science*, **150** (1992) 243–269.

[32] B. Derjaguin, V. Muller, and Y.P. Toporov, "Effect of contact deformations on the adhesion of particles", *Journal of Colloid and Interface Science*, **53** (1975) 314–326.

[33] J. Weaver, *Applications of discrete and continuous Fourier analysis*. John Wiley & Sons, 1983.

[34] H. Sone, Y. Fujinuma, and S. Hosaka, "Picogram mass sensor using resonance frequency shift of cantilever", *Japanese Journal of Applied Physics*, **43** (2004) 3648–3651.

[35] G. Kada, F. Kienberger, and P. Hinterdorfer, "Atomic force microscopy in bionanotechnology", *Nanotoday*, **3** (2008) 12–19.

[36] D. Lin, E.K. Dimitriadis, and F. Horkay, "Robust strategies for automated AFM force curve analysis — I. Non-adhesive indentation of soft, inhomogeneous materials", *Journal of Biomechanical Engineering*, **129** (2007) 430–439.

[37] M. Kopycinska-Müller, R.H. Geiss, and D.C. Hurley, "Contact mechanics and tip shape in AFM-based nanomechanical measurements", *Ultramicroscopy*, **106** (2006) 466–474.

[38] J. Liu, J.K. Notbohm, R.W. Carpick, and K.T. Turner, "Method for characterizing nanoscale wear of atomic force microscope tips", *ACS Nano*, **4** (2010) 3763–3772.